Title
Measurements of the Critical Casimir Effect and Superfluid Density in Saturated Helium-4 Films near T-Lambda

Author
Abraham, John Bishoy Sam

Publication Date
2013

Peer reviewed|Thesis/dissertation

University of California

Los Angeles

Measurements of the Critical Casimir Effect and Superfluid Density in Saturated Helium-4 Films near T_λ

A dissertation submitted in partial satisfaction

of the requirements for the degree

Doctor of Philosophy in Physics

by

John Bishoy Sam Abraham

2013

Abstract of the Dissertation

Measurements of the Critical Casimir Effect and Superfluid Density in Saturated Helium-4 Films near T_λ

by

John Bishoy Sam Abraham

Doctor of Philosophy in Physics

University of California, Los Angeles, 2013

Professor Gary A. Williams, Chair

Saturated thick films of ^{4}Helium adsorbed on a copper substrate are studied experimentally. The film thickness is measured with an ultra-sensitive capacitance bridge capable of resolving sub-Angstrom changes in film thickness. Through the use of this capacitance bridge, the critical Casimir effect in the films is studied in the vicinity of the λ transition. Additionally, the copper substrate assembly is used to generate and detect third sound in the film. Measurements are made of the third sound speed and attenuation in thick film from 1.6 K to the Kosterlitz-Thouless transition in the films. The position of the Kosterlitz-Thouless transition relative to the critical Casimir effect in the films is identified. It is discovered that the Kosterlitz-Thouless transition occurs at the beginning of the dip in film thickness due to the critical Casimir effect. When the temperature of the system is swept extremely slowly across the λ transition, a step in film thickness is observed. This step is possibly a non-universal critical Casimir effect. A model of thermal second sound excitations is developed to describe this new observation.

The dissertation of John Bishoy Sam Abraham is approved.

Konstantin I. Penanen

Hong W. Jiang

Harold R. Fetterman

Joseph A. Rudnick

Gary A. Williams, Committee Chair

University of California, Los Angeles

2013

To Lucy, Georgiana, and Sami...

Table of Contents

List of Figures

List of Tables

Acknowledgments

First, I would like to acknowledge my advisor, Gary Williams. His persistent support of my work was critical for its successful completion. Without his confidence in my ability as a scientist, it is hard to see how I could have accomplished this. I would also like to thank Konstantin Penanen our collaborator from JPL. His assistance was essential for the completion of this work and my growth as a scientist. This work was supported in part by NASA, and in part by the U.S. National Science Foundation, grant DMR 09-06467. Finally, I would like to acknowledge my wife, Kathlene. Without her support through the final stretch of this work, it would not have been possible.

Vita

1998	B.A. (Liberal Arts), Thomas Aquinas College, California.
2003	M.S. (Physics), UCLA, Los Angeles, California.
2007-2010	Commissioned Officer, United States Army

CHAPTER 1

Introduction

Recently, there has been much interest in understanding the role of finite size effects near the superfluid phase transition [17]. There are measurements confirming finite size scaling of the critical Casimir effect in films of ^{4}He [11]. As well, there are recent Monte Carlo simulations of the Critical Casimir effect for the XY model [14, 9]. The results of measurements and simulations generally are in good agreement. The main results are that the dip in the film thickness scales as predicted by finite size scaling and that there is a depression of the film thickness in the superfluid phase that may be due to bulk and surface modes in the film[18]. We have undertaken measurements of the film thickness and the superfluid density in films of ^{4}He in the vicinity of T_λ in order to identify the location of the superfluid onset in the film relative to the minimum of the Casimir dip. Monte Carlo simulations predict that the location of the Kosterlitz-Thouless (KT) transition should be somewhere between the start of the dip and the minimum [9, 15]. A previous measurement of the KT transition places it closer to the start of the dip [19]. It has even been speculated that the KT transition is in the vicinity of the dip minimum [17, 12]. The goal of this dissertation is to identify where the KT transition in the film is relative to the critical Casimir effect. Based on our measurements, the KT transition in the film is at the start of the low temperature side of the dip.

This section provides the contextual and theoretical background for our results. This review will begin by describing the Casimir effect and move on to relate some

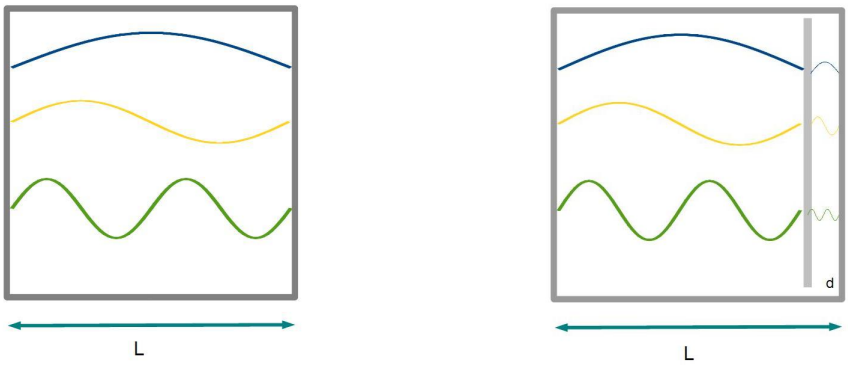

Figure 1.1: This is a diagram of the set-up for the thought experiment presented in [1]. On the left is an illustration of the box of side 'L' and it's respective modes. On the right is the box with a plate inserted a distance 'd' from one side. The introduction of the plate introduces a reduced spectrum of modes by excluding the long wavelength modes of the box.

of the fundamentals of the superfluid phase of ^{4}He. From there, we will discuss critical phenomena and finite size effects in the superfluid. Finally, all of these topics will be united in a description of the critical Casimir effect in ^{4}He.

1.1 The Casimir Effect

In 1948, H. B. G. Casimir extended his work with D. Polder on the electromagnetic interaction between a perfectly conducting plate and an atom to considering the force between two perfectly conducting plates due to zero point energy of the electromagnetic field [1] . The article presents a thought experiment involving a volume defined by perfectly conducting plates of a given size, see Fig. 1.1 for an illustration of the system. The zero point energy within the box is the sum of the zero point energy of each mode of the box, $\hbar\omega_i$. The mode structure is defined by

the size of the box and the boundary condition that the field is zero at the wall. This sum and thus the zero point energy is infinite. The next step is to consider the modes between a plate a distance 'd' from a wall. When the modes of this spectrum are given $\hbar\omega_i$ for each mode and summed, this sum is divergent as well. Surprisingly, he found that the difference between these sums is finite. As found by Casimir, the result for the difference is

$$\Delta E = -\hbar c \frac{(\pi L)^2}{24 \times 30} \frac{1}{d^3} \tag{1.1}$$

Essentially, Casimir demonstrated that removing the long wavelength modes in a region of space results in a quantifiable energy difference between that and unconfined region, even though, the zero point energy in either region is not properly defined. This effect as described by Casimir, is universal in that it does not depend on the specific material used for the boundary. There are two extensions that need to be made when considering real systems. The first extension is to consider the perfectly conducting plates at a finite temperature, this has been labeled the thermal Casimir effect. By including temperature, the spectrum of fluctuations is altered and the energy difference then becomes a function of temperature. The second extension is to consider real metal or dielectrics with surface impedance. This changes the boundary condition for the electromagnetic field. Through these extensions, the Casimir effect ceases to be universal. Much work has been done both experimentally and theoretically on the electromagnetic Casimir effect since the original article. See Refs. [20] and [21] for current reviews of this topic.

The insight that the geometric restriction of modes can lead to an energy difference can be extended to other systems, namely critical systems [22]. In critical systems it is modes of the order parameter field that are restricted. Specifically, it is the thermal fluctuations of the order parameter field that are constrained. By imposing a constraint on the fluctuations, an energy difference is created between the constrained and unconstrained regions. The electromagnetic Casimir effect

is the result of imposing a geometric constraint on quantum mechanical fluctuations. Whereas, the critical Casimir effect is the result of imposing a geometric constraint on thermal fluctuations. In the next section of this introduction, we will review the superfluid ^{4}He critical system.

1.2 Superfluid ^{4}He

Despite the simplicity of the ^{4}He atom, one of the most basic atoms. In the condensed state, it displays a fascinating range of properties which, to this day, holds properties yet to be discovered. When helium is cooled to around 4.1 K, at atmospheric pressure, it liquefies. When cooled below 2.1768 K [1], it becomes a superfluid. The history of the discovery and initial development of our understanding of superfluid ^{4}He is central to the development of Physics in the last century and has been described in many books [23, 24, 25]. We will explore some of the crucial steps in the development of the understanding of superfluidity described in the aforementioned books in order to provide context for this dissertation.

In 1908, Kammerlingh Onnes successfully liquefied Helium and the work of exploring the low temperature portion of the phase diagram began, see Fig. 1.2. When liquid Helium was cooled below 2.1768 K, it was discovered that the viscosity of the liquid when measured by capillary flow is zero. Whereas, when the viscosity was measured through the damping of an oscillating disk, it was about 10^{-5} poise. This discrepancy was explained by positing a two-fluid theory. It was first proposed by Tisza in 1940, but more fully developed by Landau in 1941. The two-fluid model posits that the superfluid phase can be understood in terms of two components; a superfluid component and a normal fluid component. The superfluid component has zero viscosity and does not contribute to the entropy of the system. While, the normal component has both viscosity and contributes to

[1] On the P90 scale.

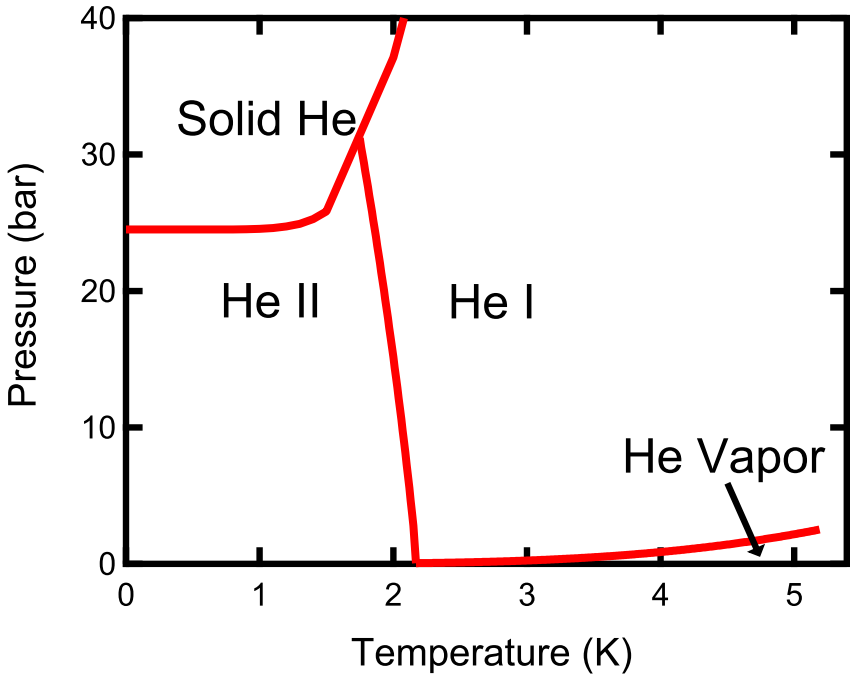

Figure 1.2: Low temperature phase diagram for Helium. He II indicates the superfluid region. The curves are generated from data found in Refs. [2, 3, 4]

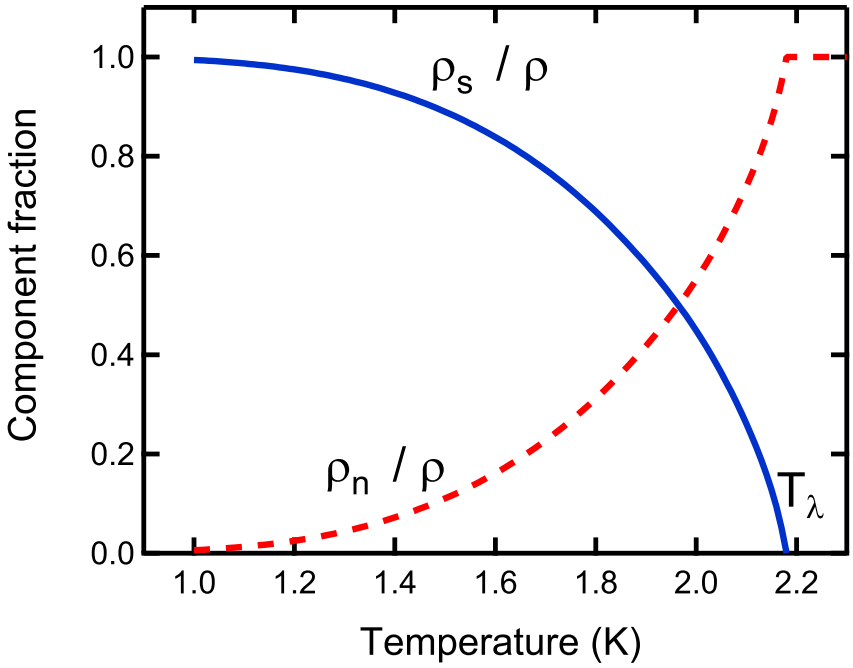

Figure 1.3: The superfluid and normal fluid component fractions versus temperature. This plot is generated using data for the superfluid density from Ref. [2].

the entropy of the system.The sum of the two components is the density of ^{4}He at a given temperature. In Fig. 1.3, the fraction for each component as a function of temperature is displayed.

In the next section, we will review the a salient feature of critical phenomena, the coherence length, which is crucial for understanding the critical Casimir effect.

1.3 The Coherence Length

As ^{4}He is cooled/heated through T_λ, it undergoes a second order phase transition which can be described as an order-disorder transition and the language of critical phenomena can be used to describe it. The order parameter becomes non-zero in the superfluid phase. It is used to describe that phase and distinguish it from

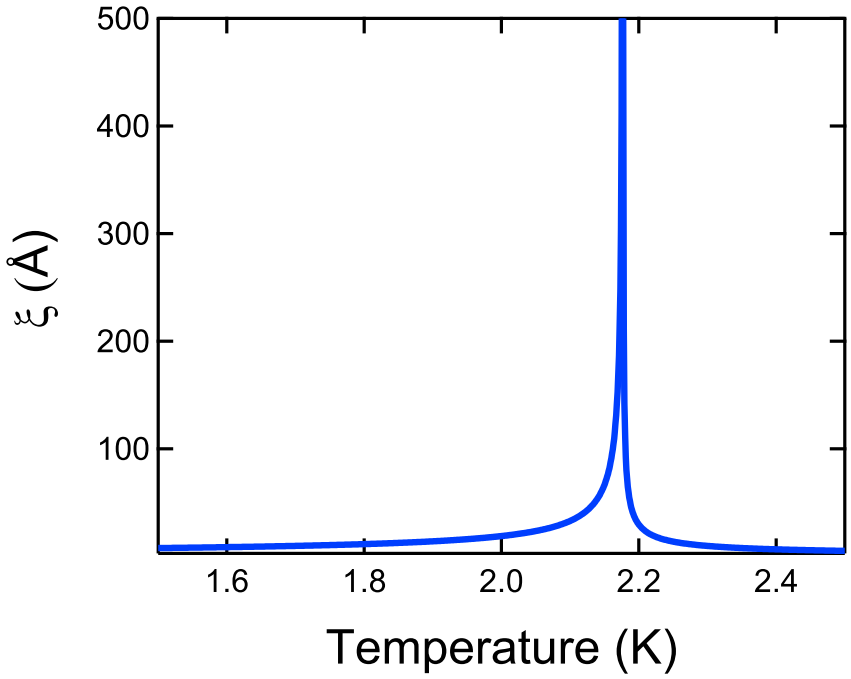

Figure 1.4: Plot of the coherence length, $\xi_{+/-}$, versus temperature.

the normal phase. The order parameter is related to the superfluid density. Close to T_λ, thermal fluctuations are able to perturb the superfluid state or order parameter on large length scales. As a sample is cooled to lower temperatures, the length scale of the fluctuations decreases according to a power law. This behavior is described by introducing the coherence length. The coherence length below T_λ is inversely proportional to the superfluid density. Thus, it is most appreciable close to T_λ. The concept of the coherence length was first developed in the mean field description of phase transitions. In that description, the role of the coherence length is to give the length scale for the order parameter to recover to it's bulk value when the superfluid is near a boundary. In that framework, it is more properly a healing length. Through the development of the renormalized group description of critical phenomena, the coherence length came to take a more prominent role[26, 27]. It describes the length scale over which the order parameter fluctuates in the bulk as well. Hohenberg et. al. describe how the correlation

length can be related to the superfluid density in Ref. [27]. The relation they find is

$$\xi = \frac{m^2 k_B T}{\hbar^2 \rho_S} \tag{1.2}$$

where m is the mass of the helium atom and the other terms have their usual meaning. In their article they also distinguish the coherence length from the healing length. They argue that although the healing length is distinct from the coherence length, it is universally related to the coherence length with the relation depending on the details of the surface effects. This distinction is important because we are interested in studying the transition in films. If the boundary can modify the effective coherence length from the bulk value, it could have relevance for the interpretation of the results. The coherence length has been measured in previous experiments in the superfluid phase, see Refs. [28] and [29]. The expression for the coherence length is

$$\xi = \xi_{+/-} \left(1 - \frac{T}{T_\lambda}\right)^{-\nu} \tag{1.3}$$

with $\xi_+ = 3.5$ Å [28], $\xi_- = 1.432$ Å [27] and $\nu = 2/3$ (the critical exponent). Since ξ_- cannot be directly measured, it is quantified by the expected ratio with ξ_+ [27]. In the next section, we will show how the coherence length can be used to describe what happens when a sample of superfluid is confined to a film.

1.4 Finite Size Scaling and the Superfluid

When superfluid helium is confined along one direction, it's behavior will depart from the behavior in bulk[30, 17]. This modification of its behavior can be described by using finite size scaling (FSS), a theory developed by M. E. Fischer. Ref. [17] provides a good review of FSS of ^{4}He. The fundamental assertion of FSS

is that the behavior of the system can be described through the scaling variable,

$$l = \frac{d}{\xi(T)} \tag{1.4}$$

where d is the length of confinement, for the purpose of this dissertation it corresponds to the film thickness. $\xi(T)$ is the correlation length. The importance of this is that there is not a 'new' coherence length for the confined system. The confined behavior can be described by scaling the same bulk correlation length by the thickness constraint. An important consequence of FFS is data collapse for thermodynamic quantities measured in films of different thickness when expressed as functions of the scaling variable, l. This is accomplished through a scaling function $\vartheta(l)$. The scaling function depends on the universality class and the boundary conditions. Additionally, the magnitude of l dictates the importance of the constraint for the thermodynamic behavior of the system. When $d \gg \xi$, the system will behave like a bulk system. When the coherence length is on the order of the film thickness, the finite extent of the system will be significant. In this dissertation, we will explore two finite size effects in helium films; the Kosterlitz-Thouless transition and the critical Casimir effect. Both of these phenomena are appreciable only when the coherence length is on the order of the film thickness.

1.4.1 Kosterliz-Thouless Transition

When ^{4}He is confined to a film, the transition temperature of the film is lowered relative to the bulk transition temperature, T_λ, the shift in transition temperature depends on the film thickness. This is well described by the vortex unbinding model of the Kosterlitz-Thouless (KT) transition [8, 31]. Their result is that the ratio of the areal superfluid density ($\sigma_s(T) = d\rho_s(T)$) and the temperature at the transition is a universal constant. The expression they find is

$$\left.\frac{\sigma_s(T)}{T}\right|_{KT} = \frac{2}{\pi}\left(\frac{m}{\hbar}\right)^2 k_B = 3.491 \times 10^{-9} g\, cm^{-2} K^{-1} \tag{1.5}$$

where m is the mass of a helium atom, k_B and $\hbar$ have their usual meanings. To place the Kosterlitz-Thouless in the context of finite size scaling theory, we can evaluate Eq. 1.2 with the KT expression (Eq. 1.5) to find l_{KT}. The result is

$$l_{KT} = \frac{d}{\xi_{KT}} = \frac{2}{\pi} \tag{1.6}$$

This results give the value of l_{KT} as being less than one. The value of l_{KT} in films of different thickness can be used as a test of finite size scaling. The primary experimental tests of this result in ^{4}He films have been made with unsaturated films far from the bulk transition[32, 33], see Table 3.1. The experimental results in this regime are in good agreement with the KT theory. The result for l_{KT} in those measurements is that $l_{KT} = 1.595(7)$. This indicates that the transition is occurring when the bulk coherence length is less than the film thickness which may allow developing our understanding of the two dimensional transition beyond a rough inequality[34]. There are a few measurements in the critical region close to T_λ. In that temperature region, films are much thicker in order to be in the superfluid regime. In the measurements which have been made closer to the bulk transition, the results have not been as conclusive [17, 35, 19] and give a value of $l_{KT} = 2.1(1)$.

On the theoretical front, early studies of the KT transition with Monte Carlo Simulations yield a value close to this [36]. Recent Monte Carlo results [15] compare well with the value from the thin film measurements. Refer to Table 3.1 for a compilation of previous results.

One of the goals of this work is to improve our understanding of the KT transition in thick films. An interesting question to investigate is whether the scaling variable ($\frac{d}{\xi_{KT}}$) at the KT transition is a constant. Does $\frac{d}{\xi_{KT}}$ scale with film

Table 1.1: Tabulation of the ratio of film thickness to coherence length at the KT Transition from different sources.

Source	$\frac{d}{\xi_{KT-}}$
Monte Carlo Simulations [15]	1.595(7)
Unsaturated Film [32, 33]	1.58(8)
Saturated Film (near T_λ)[19] [2]	2.12(10)
Confinded Helium(near T_λ) [17, 35]	2.0(1)

thickness, is there data collapse over the range of temperature from well below T_λ to the region of T_λ? As well, we could ask how does this value compare to the value of the scaling variable for other phenomena in the vicinity of the transition such as the specific heat maximum and the maximum of the critical Casimir effect[17].

1.4.2 Critical Casimir Effect

A well know property of Helium in the liquid state is that it will coat all of the surfaces of a container [24, 23, 25], see Fig. 1.5 for a sketch of the system. The equilibrium value of the film thickness, far from the lambda point, is determined by the chemical potential difference, between an atom in the bulk and on the film, being equal to zero. The atoms gain gravitational potential energy relative to the bulk by being in the film at a height above the bulk. That potential energy is balanced by the attractive Van der Waals interaction of the helium atoms to the substrate. In mathematical form, the equilibrium condition is;

$$m_{He}gh = \frac{\gamma_0}{d^3}(1 + \frac{d}{d_{1/2}})^{-1} \tag{1.7}$$

Where γ_0 and $d_{1/2}$ are constants determined by the interaction of the substrate with ^{4}He[37]. d is the thickness of the He film and h is the height of the film above the bulk. Below T_λ, it is expected that the bulk Goldstone modes and surface

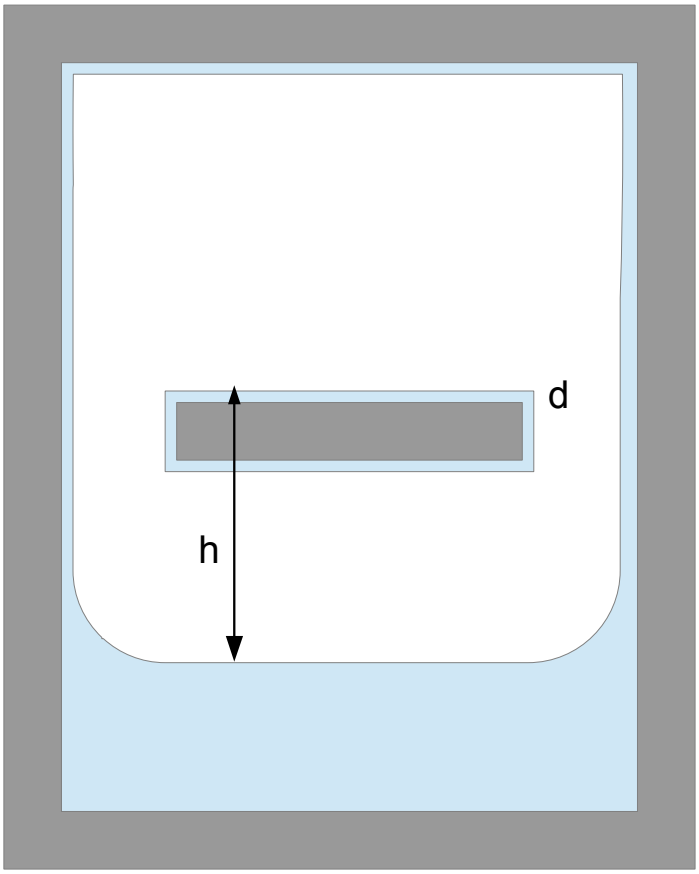

Figure 1.5: Simplified model of the experimental cell. Bulk liquid helium is in the bottom and a film coats all of the surfaces. The film thickness depends on the height of the film from the bulk.

fluctuations of the film will contribute to establishing the equilibrium thickness of the film[12]. It is expected that their contribution will lead to a constant film thinning below T_λ with an approximately 2 Å thinning for a 420 Å film. Closer to the λ point, when the coherence length is on the order of the film thickness, the critical Casimir force will become significant[22, 11, 12, 9]. The film acts to limit the spectrum of fluctuations. This leads to a free energy difference between the film and the bulk. The form this force takes is[22];

$$f = \frac{V k_B T_c}{d^3} \vartheta(d/\xi) \tag{1.8}$$

where ξ is the bulk coherence length, T_c is the transition temperature, V=45.81 Å^3/atom is the atomic volume of a helium atom, and ϑ is the Casimir scaling function. It is hypothesized that the Casimir scaling function is 'universal' in that the functional form and sign depend only on the universality class and boundary conditions of the order parameter[22]. Recent measurements confirm the universality of the Casimir scaling function[11]. The scaling function ϑ is expected to scale with scaling variable $x = l^{1/\nu} = t(d/\xi)^{1/\nu}$ [38], where $t = \frac{T}{T_\lambda} - 1$ is the reduced temperature. Equation 1.8 is included into Equation 1.7 to determine the equilibrium film thickness in the vicinity of T_λ. The result of adding the term from Equation 1.8 is to depress the film thickness from the value far from T_λ. The critical Casimir film thinning for ^{4}He films has been measured in two previous experiments [10, 11]. The more recent measurement has confirmed the validity of scaling for the Casimir scaling function. We intend to add to the information provided by the previous measures through measuring the superfluid density in the films in order to understand where the KT onset is relative to the critical Casimir film thinning. We measure the KT onset in the films through measuring the third sound onset in the films.

1.5 Overview

Before delving into our results for the critical Casimir effect, we will present our third sound results. Third sound is a surface wave acoustic mode unique to superfluid helium. Through measuring the speed and attenuation of third sound, we can characterize the films. The next chapter will begin by introducing the theoretical understanding of third sound and the relevant previous measurements. From there, we will present the relevant experimental techniques for the third sound measurements. Finally, we will present the results and discuss the insights derived from the measurements.

After the chapter on third sound, we will then present our results for the critical Casimir effect. We will summarize the theoretical and experimental results for the critical Casimir effect to date. This will provide the context for our results. Prior to presenting the results, we will describe the salient features of our experimental technique. Finally, we will present our results for the critical Casimir effect.

In this dissertation, the description of the experimental techniques and apparatus is divided between three sections. In Chapter 2, Section 3.3 the experimental techniques directly related to the third sound measurements are presented. In Chapter 3, Section **??** the experimental techniques directly related to the third sound measurements are presented. The techniques and apparatus relevant to both phenomena are relegated to Appendix A. In this way, the pertinent experimental detail is most proximate to presented results.

CHAPTER 2

Third Sound

Third sound is a propagating surface wave in superfluid helium films. It was first proposed and measured by Atkins [39]. Third sound has played an important role in understanding the properties of superfluid He films. Among the results developed through measuring third sound are an understanding of the Kosterlitz-Thouless phase transition [33] and boundary effects on the superfluid density [40, 41]. In addition to third sound being an object of study in itself, it is used in this experiment to further our understanding of the critical Casimir effect by identifying the Kosterlitz-Thouless transition temperature relative to the onset of the critical Casimir effect. This chapter will begin with a review of third sound prior to presenting the results.

2.1 Theoretical Background

Previous studies of third sound were primarily restricted to studying third sound in unsaturated films, or films far from the λ point. The more recent studies of third sound on saturated films were focused on characterizing the attenuation[42, 5]. In this thesis, measurements in saturated films where superfluidity persists to within 10 mK of the λ point are conducted in order to further characterize the phenomena and see what insights may be gleaned into the nature of superfluidity in restricted geometries.

2.1.1 Surface Waves in liquid films

Generally, surface waves will not propagate on a fluid film as thin as a saturated film of helium. This is due to the viscosity of the liquid clamping the fluid to the substrate[43]. This clamping can be understood in terms of the viscous penetration depth,

$$\delta = \sqrt{\frac{2\eta}{\omega\rho}} \tag{2.1}$$

where η is the viscosity, ω is the angular frequency of the wave, and ρ is the density. For a frequency of 100 Hz, it can be seen that for water around room temperature, the viscous penetration depth is over 100 μm and for He II around 2 K it is around 50 μm. The thickest saturated films studied are generally 50 nm or less, which is much less than the viscous penetration depth. Note that the viscous penetration depth depends inversely on frequency. Thus, at high frequency the viscous normal component can become decoupled from the substrate and can be driven. That is not a concern for the experimental regime of the measurements reported here, since the frequencies we work with for third sound are all below 100 Hz. So the normal component is 'locked' to the substrate in the frequency regime for these measurements. We are interested in shallow wave modes. So, the expression for a surface wave whose wavelength is much longer than its depth is[43]

$$\nu^2 = \left(\frac{f\lambda}{2\pi} + \frac{2\pi\sigma}{\rho\lambda}\right) tanh\frac{2d\pi}{\lambda} \tag{2.2}$$

where ν is the phase velocity, f is the Van der Waals acceleration of the film by the substrate, λ is the wavelength, σ is the surface tension, and d is the film height. Since the argument of the hyperbolic tangent is much less than one, it can be approximated as the argument. We can further simplify by ignoring the term with surface tension since that term is a factor of 10^5 smaller than the Van

der Waals term. The simplified expression for the surface wave becomes,

$$\nu^2 = fd \tag{2.3}$$

Since the surface wave is only appreciable in the superfluid phase, the superfluid fraction is included in the dispersion relation. Then the expression becomes,

$$\nu^2 = \frac{\bar{\rho}_s}{\rho} fd \tag{2.4}$$

The bar placed over ρ_s distinguishes it from the bulk value of the superfluid density, since it can be expected that boundary effects will depress the value of ρ_s from the bulk value. This topic will be addressed in section 2.1.3. As well, this expression for the dispersion relation is only partially correct. Measurements of third sound show that there is significant attenuation, and a contribution to the real part of dispersion relation from the evaporation-condensation mechanism underlying its propagation. These issues will be addressed in the following section as we further develop the dispersion relation.

To further develop our understanding of the dispersion relation, we must being with the model of two fluid hydrodynamics. Since the superfluid component is in motion, while the normal fluid is clamped down, there will be changes in local density of superfluid that will propagate with the wave. This in turn will lead to a modulation of the local temperature that will accompany the motion of the superfluid. This temperature oscillation will, in turn, lead to evaporation in the hotter regions and condensation in the cooler regions. This evaporation-condensation mechanism is needed to refine our model. Additionally, it will also be the means that we will initially incorporate attenuation in the model of third sound. In the next sections, we will examine the two primary descriptions of third sound.

2.1.2 The Atkins and Bergman Models

In an effort to understand the surface tension of He II, Atkins[39] predicted that surface waves could propagate in the film even though it is thinner than the viscous penetration depth, see Eq. 2.1. He derived a dispersion relation for third sound from three expressions; conservation of mass, expression of the heat flow, and an equation of motion for the superfluid component based on the two fluid model. For conservation of mass, he considers that the mass of an element can change due to evaporation/condensation or superfluid flow. For the heat flow,that arises from the latent heat of evaporation/condensation and the flow of the superfluid component. Finally, the equation of motion for the superfluid has the superfluid acceleration proportional to the gradient of the pressure at the surface, with contributions from Van der Waals and the vapor pressure. This model leads to the following complex dispersion relation

$$\frac{\omega^2}{k^2} = \frac{\bar{\rho_s}}{\rho} f d + \frac{\bar{\rho_s}}{\rho} ST \frac{[(S - \frac{\beta}{\rho}) - i\frac{Kf}{\rho\omega}]}{(C - i\frac{KL}{d\rho\omega})} \tag{2.5}$$

Where C, S, and L are the specific heat, entropy, and the heat of vaporization per gram. β is the slope of the vapor pressure curve. K is mass change per unit temperature for the evaporation mechanism. In the limit that the frequency goes to zero, the dispersion relation becomes,

$$\frac{\omega^2}{k^2} = \frac{\bar{\rho_s}}{\rho} f d (1 + \frac{TS}{L}) \tag{2.6}$$

This is what is cited as Atkins' dispersion relation. The salient point of it is that C_3 is proportional to $(1+\frac{TS}{L})^{\frac{1}{2}}$. His model is somewhat of an oversimplification that is valid in certain limits. Bergman discovered that including the substrate and a more complete model of the vapor coupling gives a more complete picture of third sound.

Bergman's model[44, 7] diverges from Atkins in the choice of equations to formulate the dispersion relation. The primary point of departure is in Bergman's choice of the Onsager reciprocity relations[45] to model the thermodynamics of the evaporation-condensation process; as well in his choice of including thermal coupling to the substrate and coupling to the sound modes in the vapor. Bergman's model also takes into account the thermal conductivity of the substrate.

Bergman gives a general solution for the third sound dispersion relation, which is a practically intractable expression with more than ten terms. He simplifies the expression by taking a thin film and a thick film limit. In the thick film limit the coupling to the substrate and the vapor is not significant. The thick film limit is valid for films greater than 70 nm. Thus, the films that we study in this experiment are less than the thick film limit so including the coupling to the substrate and the vapor are critical for studying the dynamics of third sound in the films we are working with.

Since Bergman's model includes the dissipative effects of the third sound wave coupling to the substrate and the vapor, it generates a greater value for attenuation than Atkins's model. Bergman's model has better agreement with experimental measurements with thin films at low temperatures [42, 5], although it still underestimates the attenuation by more than an order of magnitude. Our experiment will allow us to see how well it describes the thick film attenuation closer to T_λ. Bergman's model also leads to a difference in the real part of the dispersion relation from that of Atkins, adding another power of $(1+\frac{TS}{L})$, the term accounting for the vapor exchange. The expression for the real part of the dispersion equation then becomes;

$$\frac{\omega^2}{k^2} = \frac{\bar{\rho_s}}{\rho} f d (1 + \frac{TS}{L})^2 \tag{2.7}$$

The attenuation of third sound is proportional to the imaginary component

of the dispersion relation. We will not reproduce the equation describing that here because it is quite long. The interested reader is directed to the work of Bergman[44, 7] for those expressions. The attenuation of third sound has been the focus of much attention from the beginning of the measurements of third sound. A main reason for this interest is that the measured value of attenuation exceeds the predictions of the Bergman model. Over the years, theories have been advanced to describe the anomalous attenuation[46, 47, 48]. Recent measurements of third sound attenuation have confirmed the anomalously high value of attenuation in thick films[5, 49]. Our measurements agree with the recent work. In addition, we extend the range of measured values of attenuation to the λ point.

2.1.3 Depletion of $\frac{\rho_s}{\rho}$

In the context of the Ginzburg-Pitaevski mean field description of superfluidity[50], it is expected that the superfluid density should be depressed from the bulk value a certain distance from a wall[40].This depression is described in terms of a healing length[50, 40, 27]. The healing length is thought to be proportional to the coherence length. The factor of proportionality depends on the boundary condition of the superfluid wave function at the surface. It takes the value of 2 if the wave function goes to zero and square root of two if the derivative is zero at the surface[40].

Additionally, the pressure in the film within a few atomic layers of the substrate will exceed the solidification pressure of He. This will lead to the first layers of He on the substrate being solid. As well, once the temperature of the system is above the lower lambda point (1.76 K), there will also be a certain thickness of Helium above the solid layer where the superfluid density will be zero due to the pressure exceeding the pressure along the λ line. As the temperature progresses to the λ point, this thickness will continue increasing. Since these pressure effects depend on the Van der Waals effect, the contribution of the solid layer and pressure-

quenched normal layer will depend on the substrate used. For example, these effects will be far more pronounced in copper than in glass substrate by a factor of 2.36 which is the ratio of the Van der Waals coefficient for the two materials.

These effects have been integrated into various depletion layer models[40, 41, 51, 52] developed over the span of years. These models posit a 'dead layer' to correct the superfluid density. Thus the superfluid density in equation 2.7 is distinct from the bulk superfluid density. They are related through the dead layer, known as 'big D'. The expression is

$$D = D_{solid} + D_{normal} + \xi_{healinglength} \tag{2.8}$$

D is composed of three terms; the solid layer, the normal layer, and the boundary supppression expressed through the healing length. We can now express $\frac{\overline{\rho_s}}{\rho_s}$ in terms of D;

$$\frac{\overline{\rho_s}}{\rho_s} = (1 - \frac{D(T)}{d}) \tag{2.9}$$

where D is explicitly shown to be a function of temperature and d is the film thickness. The temperature dependence of D is primarily through the coherence length and the normal layer size. The dead layer has been investigated experimentally in unsaturated films[40, 41]. This thesis is the first investigation concerning depletion in thick films to the vicinity of T_λ. As such, it provides new insight to the modification of the superfluid density through proximity to a surface. Before reporting the results, the experimental methods used to study third sound in this experiment will be described.

2.2 Experimental Methods

Surface waves on films of helium can be generated and detected using a capacitance technique described in Refs. [53, 5]. In the this section, we will outline the experimental methods used for these measurements with our system. This section will begin with a description of the cell. After the cell is described, the measurement techniques used will be reviewed. A complete description of the cell and the general features of the experiment are contained in Appendix A.

2.2.1 The Experimental Cell

With the system, we are able to measure sub Å resolution for ^{4}He film thickness changes and have 10 μK temperature resolution. The primary components of the cell relevant for this set of measurements are the electrode assembly and the λ stage. The electrode assembly contains the substrate for the helium film. The substrate forms a capacitor with the helium films on each terminal and the vapor in the gap contributing to the effective dielectric constant defining the capacitor.

Previous work has illustrated the importance of the surface quality of the substrate for He film measurements [10, 54]. After rough machining of the electrode surfaces, they are sent out for diamond turning to a manufacturing firm[1]. Diamond turning is a surface finishing technique which can achieve a surface roughness on the nm scale. From AFM measurements, we estimate the surface roughness to be 10 nm. The cell body and all subcomponents which require high thermal conductivity are manufactured from OFHC Copper. The substrates consist of rectangular electrodes in a grounding assembly to minimize the fringing field of the capacitor. The assembly consists of one large electrode facing four quadrant electrodes across a gap of 60 μm, see Figure 2.1 a for schematic. The quadrants are separated by a grounding cross and the gap between the monolithic

[1]KAF Manufacturing Stamford, CT

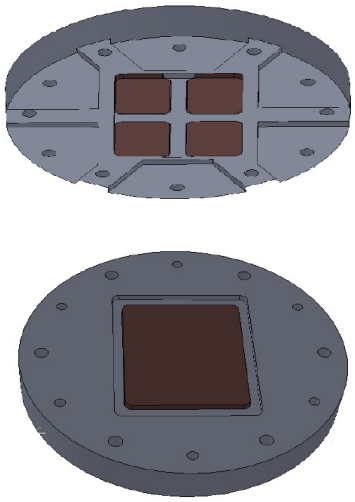

Figure 2.1: Exploded view of the electrode assembly. All parts are fabricated from OFHC copper. The electrode holders are shaded gray to indicated that the electrodes are not electrically connected to the holders.

electrode and the quadrants is set by a Kapton film 60μm thick. The area of the quadrant electrode is around 1 cm^2, this results in a capacitance of approximately 15 pF for a quadrant electrode to the ground electrode. The actual value of the capacitance is not critical for the third sound measurements since the third sound signal arises from the change in capacitance. The discussion of that experimental detail will be relegated to the section on film thickness measurements for the critical Casimir effect, Section 3.3. This assembly is sealed in our cell by attaching the assembly to the main flange of our cell and sealing the flange to the cell body with an indium seal. Electrical connections to the electrodes are passed out of the cell through homemade coaxial epoxy seals using a recipe from Ref. [55].

The lambda stage is for the purpose of accurately establishing the position of T_λ in our system. I will briefly discuss it here and leave a more thorough discussion for the section in the appendix on the cryostat. It consists of an OFHC copper block and a 1/4" thin-walled stainless steel tube connecting to the bottom of the

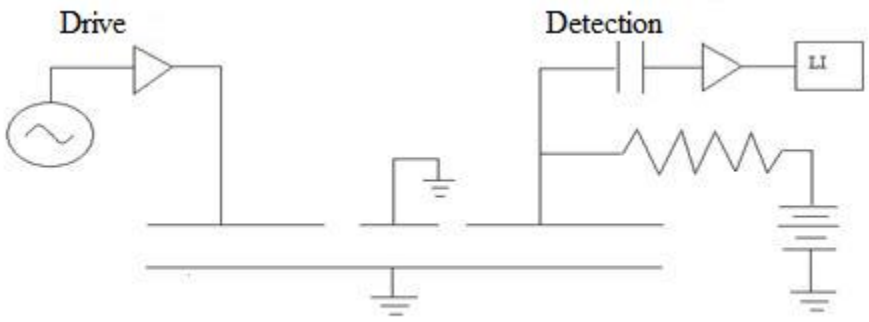

Figure 2.2: Charged Bias Third Sound Circuit. The output of a lock-in drives a quadrant on the left. On the right, the quadrant is charged through a large resistor to act as a microphone. The change in film thickness is detected by the lock-in via the capacitance change.

cell. Attached to the copper block is a heater and thermometer. The stainless steel tube is our reservoir of bulk He for the cell. When the bulk He in the stage goes through the transition, the thermal conductivity between the thermometer on the bottom of the stage and on the cell changes dramatically. This can be seen as relative change in the slope of the readings of the thermometers. Utilizing this stage, I can determine T_λ to within 10 μK.

2.2.2 Third Sound Generation and Detection

In this experiment, third sound waves in the ^{4}He film are detected using a charge bias technique developed by Hoffmann et al.[5]. Figure 2.2 is a schematic of the detection and generation scheme. One quadrant is driven by the output of a lock-in amplifier. Another quadrant is charged with a 100 V battery[2] through a large resistor (1GΩ) to keep the charge on the electrode constant during our measurement interval. Since the charge is constant, a change in capacitance will result in

[2]Charging the gap above 120 Volts leads to breakdown in the vapor.

a change in voltage at the pre-amp input. This voltage is then detected at the second harmonic of the drive since the response will go as the square of the drive and thus twice the drive frequency. The typical settings for the instrumentation and the geometry of our cell result in a sensitivity of 1 mV corresponding to 0.1 Å of film change. In Figure 2.3 a representative third sound data set is reproduced. Third sound is studied in this system by allowing the cell to thermally equilibrate to a given temperature, sweeping the frequency of the lock-in amplifier drive, and detecting the response at the second harmonic. In the next section, I will describe how the frequency sweep is used to characterize the third sound response of the film at a given temperature.

2.2.3 Third Sound measurements

The third sound resonator has a rectangular symmetry, and if the wave amplitude falls to zero at the boundaries, the resonant frequencies will be

$$\begin{gathered} \omega_{m,n} = c_3 k_{m,n} \\ k_{m,n} = \sqrt{\left(\frac{m\pi}{L_x}\right)^2 + \left(\frac{n\pi}{L_y}\right)^2}\; m,n = 0,1,2,3,... \end{gathered} \tag{2.10}$$

The geometry of the resonator determine both L_x and L_y. The values of L_x and L_y are 2.8 and 2.2 cm, respectively. By fitting the peaks of the frequency response curve to Lorentzian peaks, we can extract the resonant frequencies at a given temperature. As can be seen in Figure 2.3, there are more resonances detected than those predicted with the dispersion relation of 2.10. This is probably due to the having additional reflecting boundaries other than the outside border of the large electrode. For example, there are the boundaries defining the quadrant electrodes. Only the first three modes which are clearly related to the primary boundaries of the large electrode are tracked from the base temperature of our cryostat to the vicinity of T_λ. In this way, for each temperature step, three measurements of c_3 are made, see figure 2.4. Using equation 2.7, we can solve

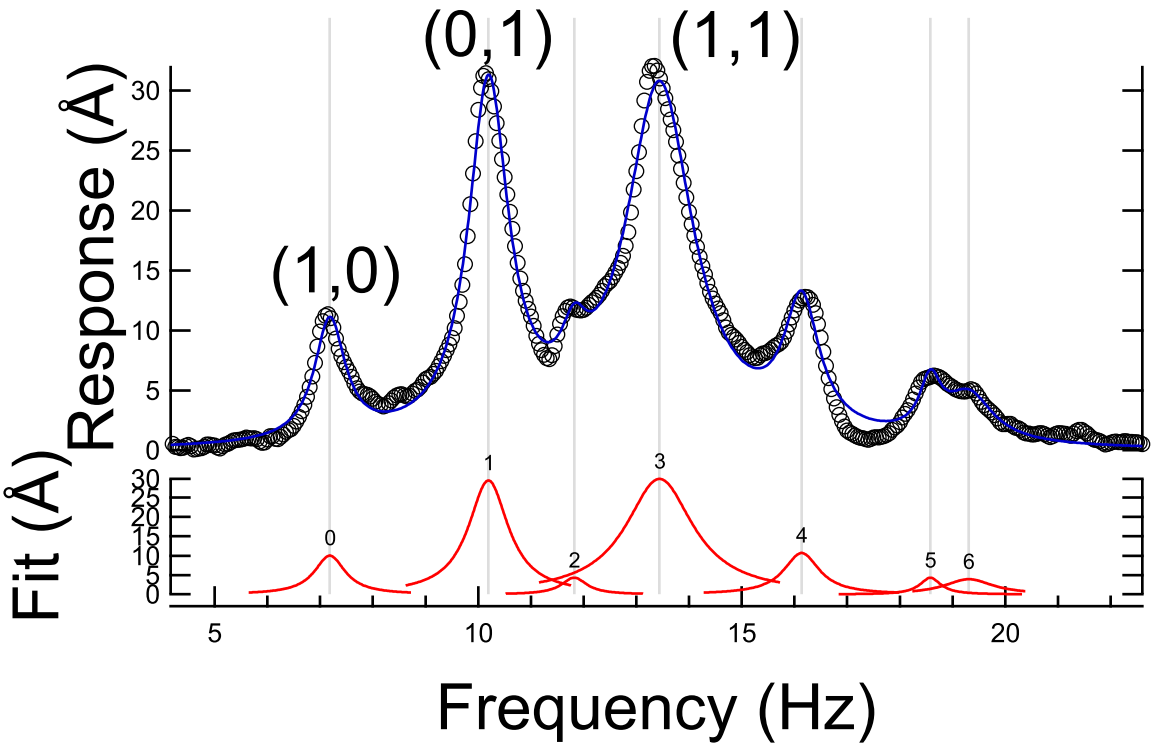

Figure 2.3: 480 Å film third sound sweep data with Lorentzian fits to the peaks. The cell temperature during the sweep is 1.600 K. The first three prominent modes correspond to the (1,0), (0,1), and (1,1) modes. These modes are tracked to the vicinity of the λ point.

for the film thickness in terms of the Van der Waals force, third sound speed, superfluid density, and the evaporation correction. A frequency sweep of third sound close to the base temperature is used to establish the film thickness, see figure 2.3. Using the measured third sound speed, the superfluid density from Ref. [2], and other terms, we get a measurement good to about five percent of the film thickness. The dominant uncertainty is the value of the Van der Waals force for our substrate. We calculate the Van der Waals force based on the retarded expression from E. Cheng and M. W. Cole[37].

2.3 Results

Experiments were conducted on five different film thicknesses; 27, 30, 30.5, 34.4, and 48 nm thick. For each film we stepped the cell in temperature and then took a frequency sweep to measure the film response. The temperature range of our data spans from the base temperature, 1.6 K, to the vicinity of the λ point. From the measurements of third sound resonances as a function of temperature, we can understand the attenuation of third sound and the superfluid density as a function of temperature. Additionally, we can measure the temperature and areal superfluid density at the Kosterlitz-Thouless transition in the films. The results of these measurements are presented in this section.

2.3.1 C_3 versus Temperature

In Figure 2.4, the third sound speed as a function of frequency is plotted for each film. The third sound speed is calculated from the resonant frequency by multiplying by the wave number. According to Equation 2.7, the speed of the wave should decrease as the film thickness grows, at a given temperature. This behavior is observed in the measurements. The only previous measurements of third sound in saturated films as a function of temperature are from Refs. [5, 6, 49].

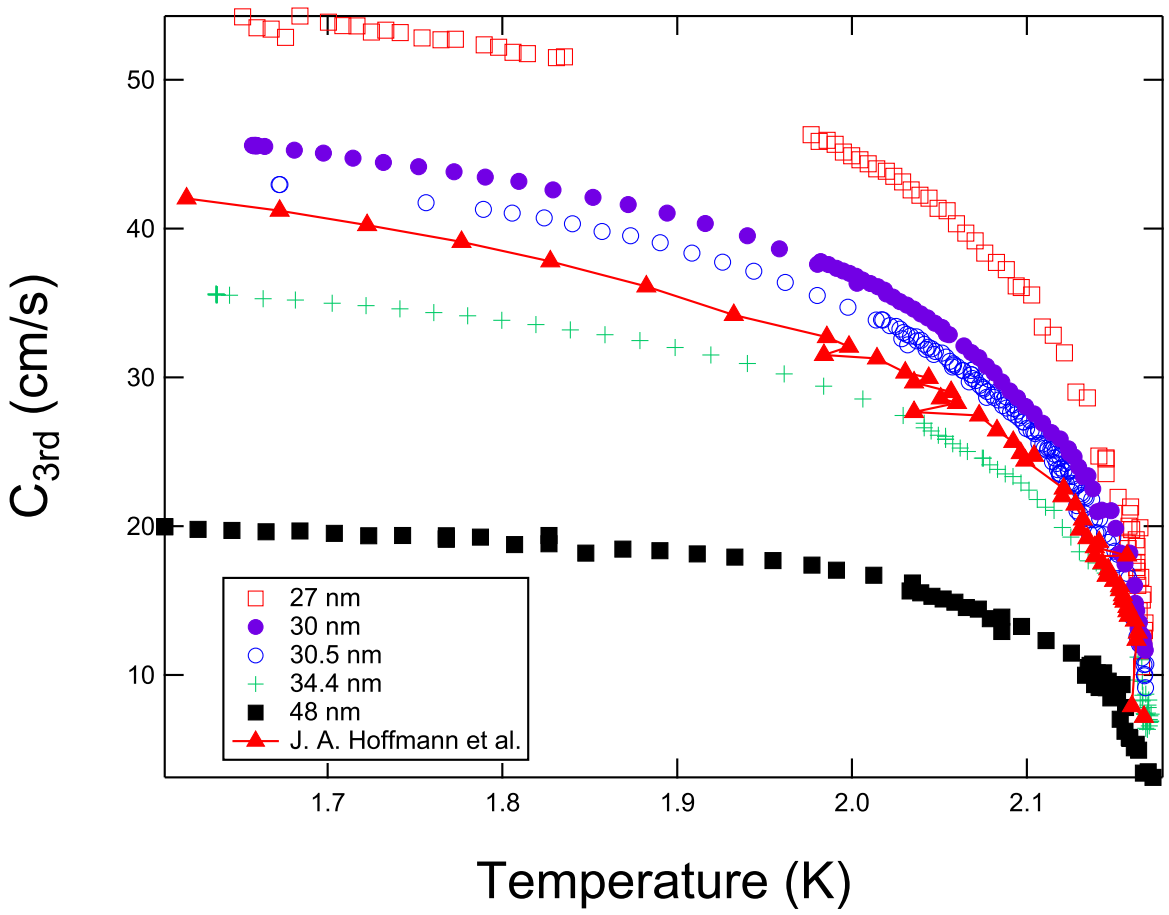

Figure 2.4: Third sound speed versus temperature for the films studied. Each data point is the average of c_3 measured for each of the first three resonant modes. For comparison, we calculate c_3 from the data provided in [5].

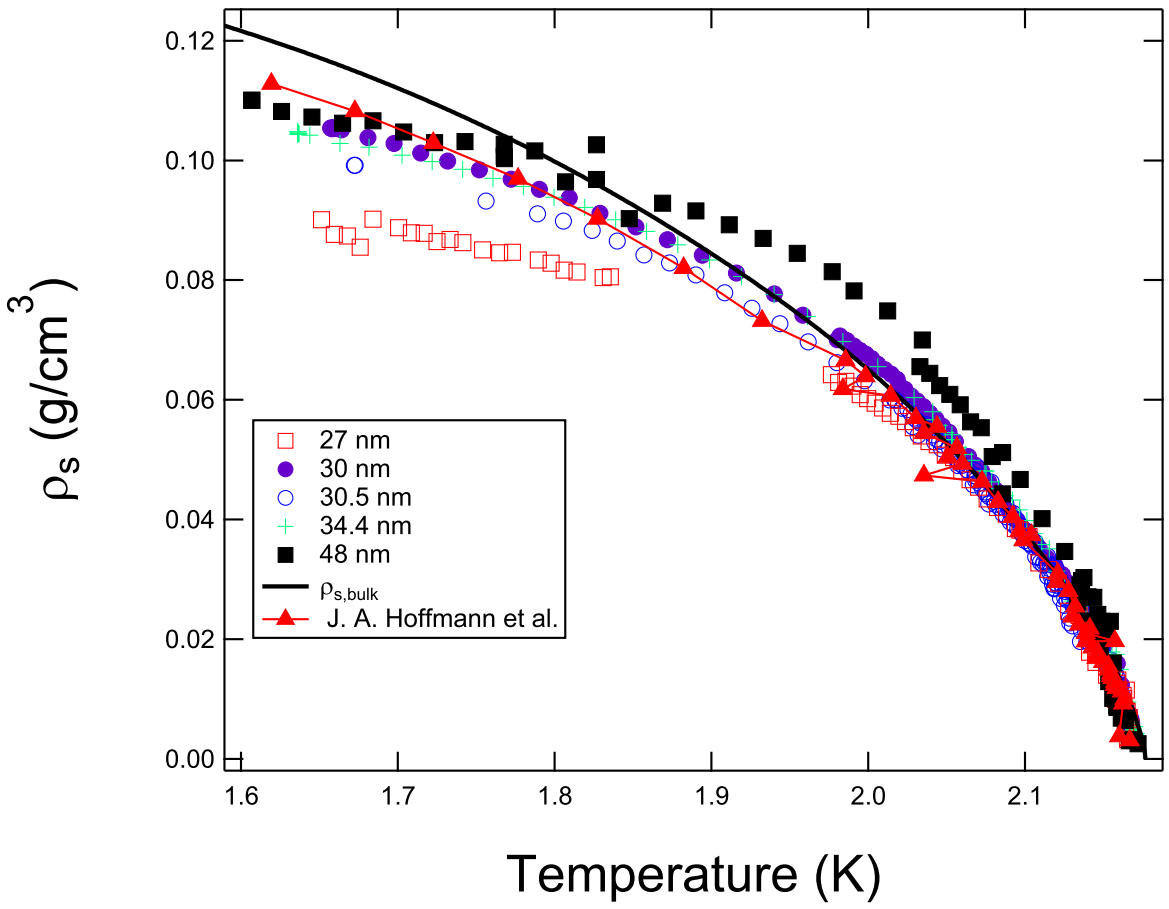

Figure 2.5: The superfluid density derived from measurements of the third sound speed is displayed against the bulk superfluid density from [2] and the results from previous measurements by J. A. Hoffmann et al.[5].

These measurements are included in Figure 2.4 for comparison. As can be seen in the figure, the dominant temperature dependence of the third sound speed is the superfluid density, see equation 2.7. This allows the use of third sound as a sensitive probe of the superfluid density in films.

2.3.2 $\frac{\rho_s}{\rho}$ versus Temperature

From the third sound speed, the superfluid density in the film can be calculated using Equation 2.7. In Figures 2.5 and 2.6, the result is presented along with the

bulk value of the superfluid density from the tables of Donnelly and Barenghi[2] for comparison. As well, calculated values for $\bar{\rho}_s$ from the data of J. A. Hoffmann et al. [5] are included. For their data, we assumed a film thickness of 32 nm and adjusted the value of wave number to match the expected value of C_3 at low temperature. The boundary condition for the experimental set-up used in [5] is not well defined[3]. The wave number is adjusted through dividing by a factor of 2 to match the expected value for the third sound speed for a 32 nm film using Equation 2.7. With those corrections, the agreement is quite good with our measurements. There is general agreement between the bulk value of the superfluid density and the measurements of the superfluid density from the third sound speed. Equation 2.7 does not account for the depletion of the superfluid density due to the substrate.

By examining Figures 2.5 and 2.6, we can see a discrepancy at low temperature and close to the λ point between the bulk superfluid density and the superfluid density measured via third sound in both sets of experimental data. The discrepancy close to the lambda point is due to the vortex-unbinding suppression of the superfluid density, described in the Kosterlitz-Thouless theory developed by V. Ambegaokar et. al. [34]. The role of the boundary induced superfluid depletion in the measurements can be more easily visualized by scaling the measurement of the superfluid density with the bulk value. This is plotted in Figure 2.7. In the plot, we included the results of the calculation of the depletion layer correction to the superfluid density for a 30 nm film as described in Appendix B. There is good agreement between the data and the depletion model far away from and close to the λ point.

The agreement fails from 1.85 to 2.15 K and indicates that the superfluid density in the film recovers to the bulk value or even exceeds it. The largest film thickness studied, 48 nm, shows a larger value of the superfluid density in

[3]Private Communication with K. Penanen

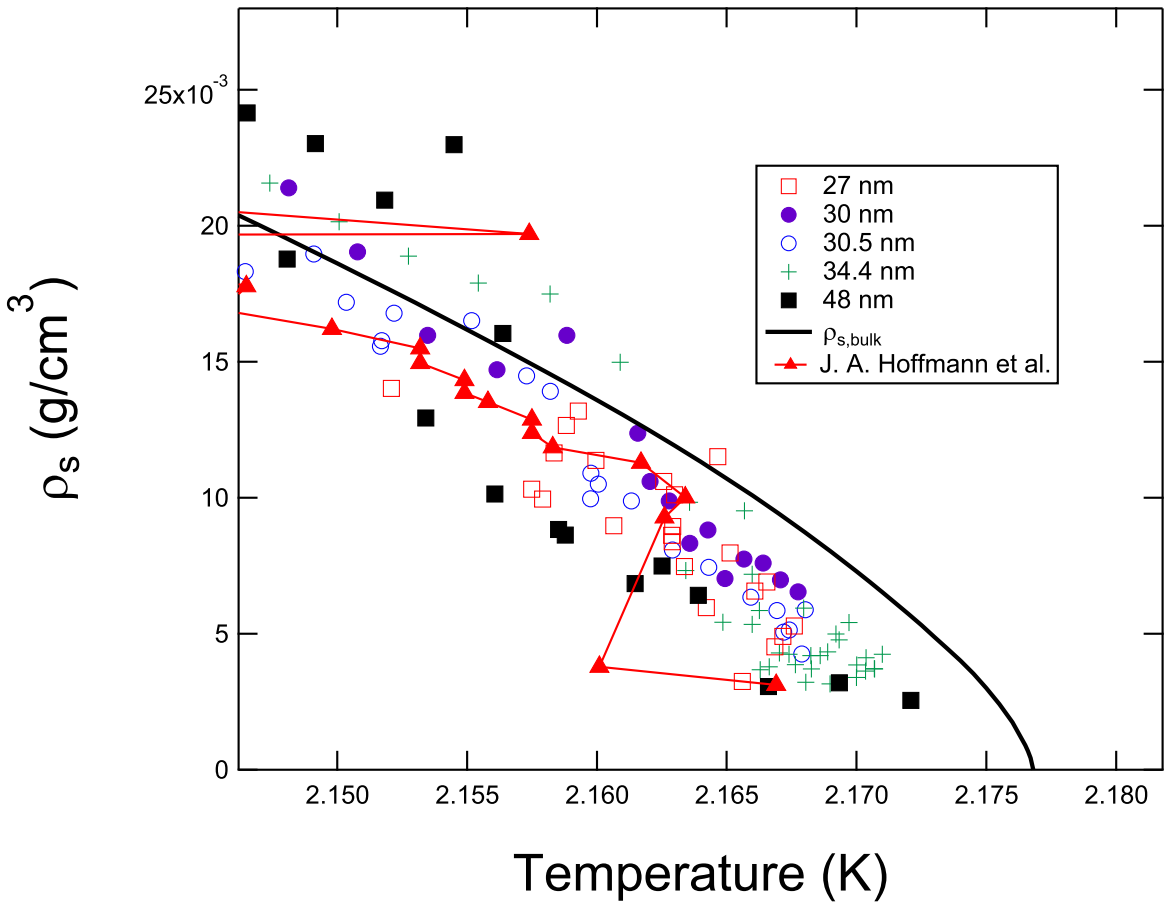

Figure 2.6: Blow up of Figure 2.5 in the vicinity of the λ point.

the film than the bulk starting around 1.9 K. This is seen in all of the resonant modes tracked for the film. This disagreement may be explained through the anisotropy in the superfluid density which is expected to develop in films[56]. The superfluid density in the perpendicular direction to the substrate exceeds the bulk superfluid density in vortex loop simulations starting well below the region of vortex unbinding, around 50 mK from the transition temperature for a 12 nm film. In a paper by Williams [56], the calculation is performed for a film thickness of 121 Å and shows enhancement of the perpendicular component more than 50 mK from the vortex unbinding region. How that enhancement scales for thicker films could explain what is occurring in the thicker films. The current models of third sound assume that the superfluid density is isotropic. Our measurements indicate that assumption may be false. A reformulation of the third sound model in terms of an anisotropic superfluid density may resolve the discrepancy between our measurements and the current model of depletion.

2.3.3 α_3 versus Temperature

From the third sound speed and the quality factor of the fits to the response peaks (Figure 2.3) we can calculate the third sound attenuation using the expression

$$\alpha = \frac{\omega_3}{2QC_3} \tag{2.11}$$

In Figure 2.8 we display the results of our measurement of attenuation along with recent measurements of attenuation in saturated films[6] and the expected attenuation from Bergman's thermohydrodynamic model for a 30 nm film. The attenuation we measure in our films are a factor of 100 times great than his model predicts. Contributing to that difference is the attenuation due to the transmission of third sound wave at the boundary, see Appendix C. Our measurements of attenuation agree with the measurements of K. Penanen et. al [6]. At 2.1 K,

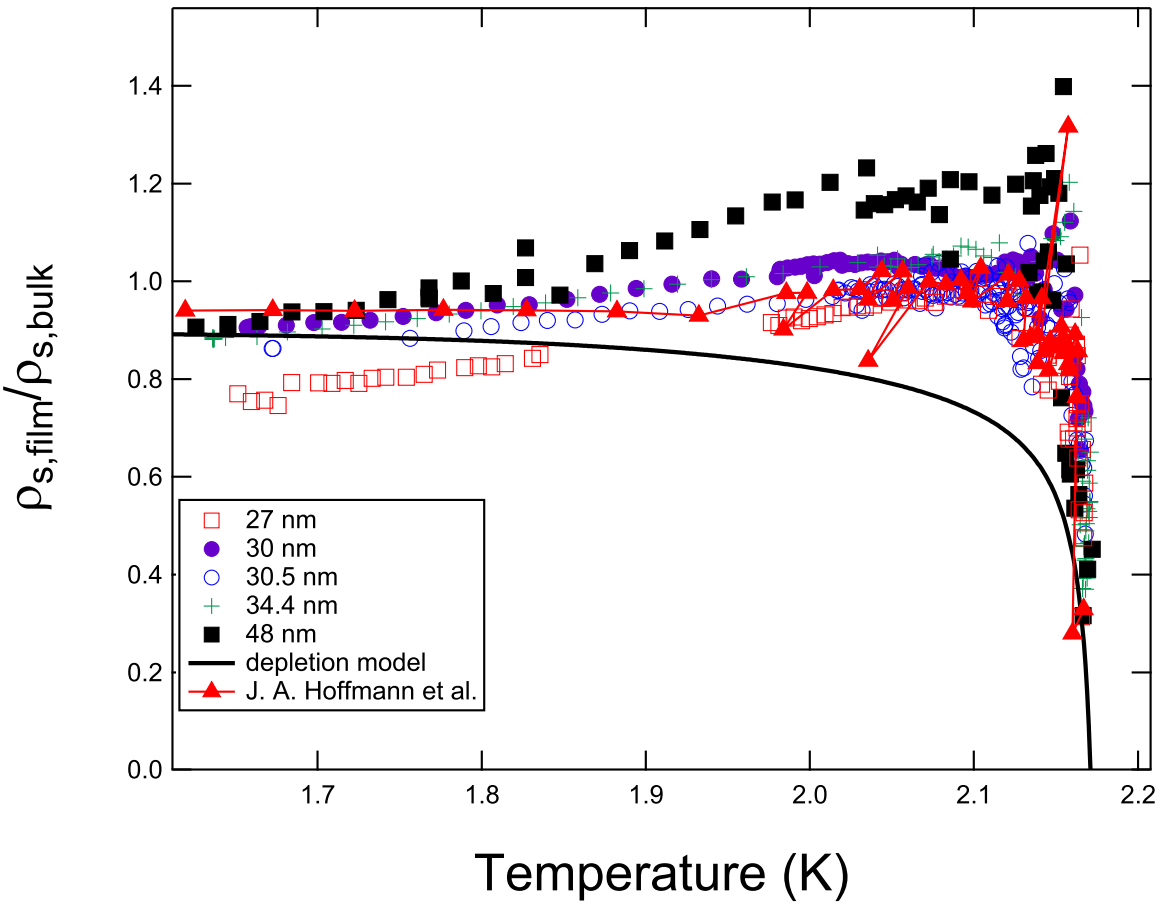

Figure 2.7: The measured superfluid density from the third sound speed scaled by the bulk superfluid density from [2]. The black line represents the depletion model developed in Appendix B. The measured results depart from the model in the central region.

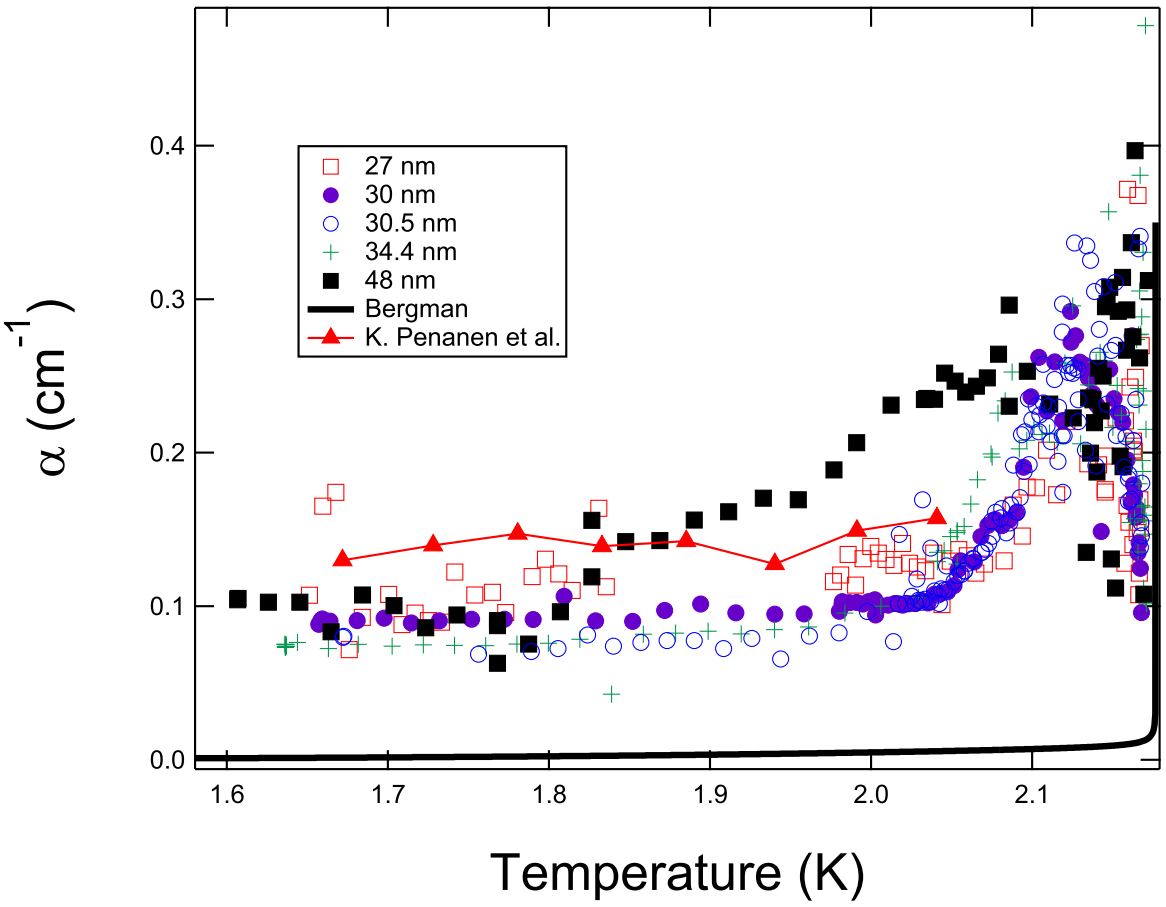

Figure 2.8: Attenuation results plotted with the results from [6] and the expected attenuation for a 30 nm from [7].

the attenuation begins to increase and peaks at 2.134 K for most of the films measured. This increase is not reflected in the attenuation model of Bergman or the model developed to describe the attenuation due to the boundary in Appendix C. From the peak at 2.134 K, the attenuation drops back to the low temperature value. It is unclear what is causing the rise and fall in attenuation. It is not due to the Thermohydrodynamics of Bergman nor is it described in the Boundary model of attenuation. As well, the model of third sound attenuation described by V. Ambegaokar et. al. [34] due to vortex unbinding is appreciable only 10 mK from the λ point. Interestingly, the attenuation peak occurs in the same temperature region where the depletion model fails. The attenuation of third sound may be enhanced by the anisotropy in the superflud density. This possibility is compelling since the superfluid density in the perpendicular component should determine the attenuation in the film far more strongly than in the parallel direction because of the critical role evaporation plays in attenuation of third sound.

2.3.4 KT transition as measured by third sound

From the third sound data we can measure the temperature and the areal superfluid density at the Kosterlitz-Thouless transition in the films, T_{KT} and $\rho_s d$, respectively. The KT onset temperature is the temperature third sound ceases to propagate in the film under investigation. The superfluid density at the KT point is measured through measuring the third sound speed at the transition. The third sound cutoff in He films provided some of the earliest confirmation of the KT theory [33, 57].

Measurements are made by stepping in temperature and conducting a sweep in frequency to see the resonant response of the film. In addition to the amplitude response of the film,we are able to measure the phase response, see Figure 2.9. We follow both the amplitude and phase of the film as T_{KT} is approached from below and above. Using this method, we are able to determine T_{KT} to within

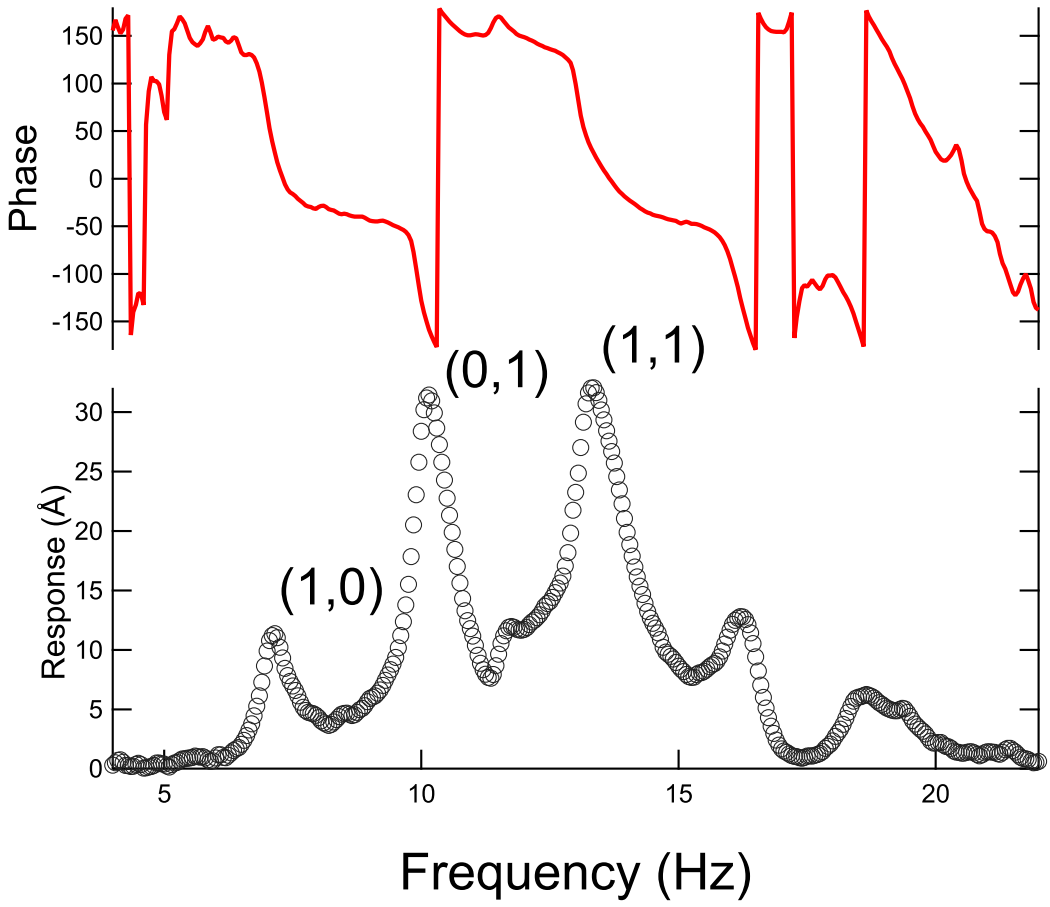

Figure 2.9: This is a plot of the phase and amplitude response. This is the same sweep as presented in Figure 2.3. The phase response of the films complements the ampletude response. It facilitates in the identification of the KT transition for the films.

L (Å)	270	300	305	344	480
T_{KT}	2.167	2.1676	2.168	2.171	2.172

Table 2.1: Summary of results for the Kosterlitz-Thouless temperature of the films studied.

0.5 mK. By using equation 2.7 and a sweep of the third sound resonances at the base temperature, we are able to vary precisely measure the film thickness. We estimate that the uncertainty in film thickness is comparable to the uncertainty in the value of the Van der Waals coefficient, which is generally the dominant source of uncertainty in determining the thickness of He films [10, 37]. Our uncertainty in the film thickness is approximately 5 percent. The uncertainty in the onset temperature is less than .5 mK. The uncertainty in the film thickness dominates over the uncertainty in temperature or the location of T_{KT} by an order of magnitude. Our results for each film are listed in table 2.1.

In addition to measuring T_{KT} of the films, we measure σ_s of the films at the KT transition, in order to ensure that the KT transition is being measured and not simply losing signal in the noise, see Figure 2.10. The result for all of the measurements is $\frac{\sigma_s}{T_{Kt}} = 4.7 \pm 1.5 \times 10^{-9}$g cm^{-2} K^{-1} which is in agreement with previous measurements and the theoretical value, $\frac{\sigma_s}{T_{Kt}} = 3.49 \times 10^{-9}$g cm^{-2} K^{-1} [8, 31, 33, 32]. Recent measurements using Adiabatic Fountain Resonance give a value of $\frac{\sigma_s}{T_{Kt}} = 4.5 \times 10^{-9}$g cm^{-2}K $^{-1}$ [35] in agreement with the current measurements.

We can now return to the question of what insight our results give for finite size scaling of the KT transition, see Section 1.4. We can calculate ξ_{KT} from the T$_{KT}$ we measure for each film using Equation 1.3. For the films we have measured, our result is $\frac{d}{\xi_{KT}} = 2.13 \pm 0.1$ which is in good agreement with previous measurements of the KT transition in thick films [17, 35, 19], but not in agreement with thin film measurements and Monte Carlo simulations, see Table 3.1. Assuming the validity

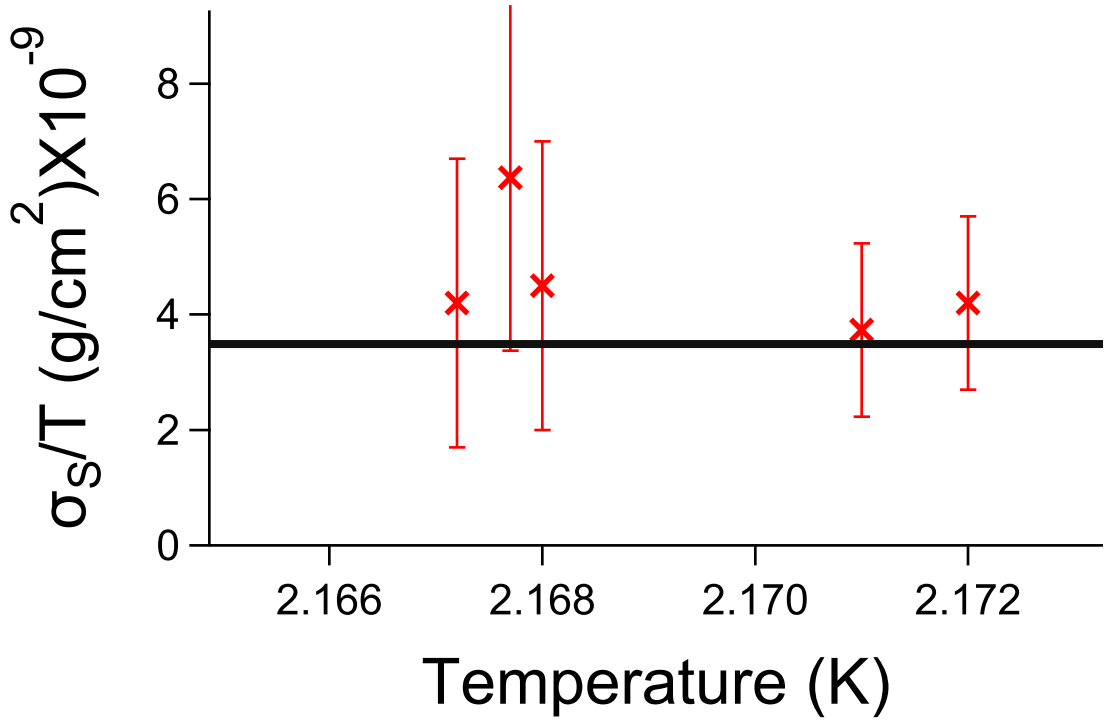

Figure 2.10: Here is the value for the areal density divided by the transition temperature of the films. The solid line is the universal value from [8].

of finite size scaling, we can conjecture as to why there is a difference in $\frac{d}{\xi_{KT}}$ for thin versus thick films.

It is plausible that we are seeing the KT transition at lower temperature because the depletion layer gets to the size of the film thickness before the film can get to the KT transition at a higher temperature relative to the film thickness as it does in the unsaturated film measurements and the Monte Carlo simulations. Given the uncertainties in the model of depletion, a better model of the depletion layer needs to be developed in order to understand more completely why there is this discrepancy between the results far from and near T_λ. As a first step, a model of the depletion layer is developed in Appendix B. It is possible that the depletion layer in thick films modify the surface effect such as to modify the ratio of the healing length to the coherence length according to Reference [27].

2.4 Discussion

In this chapter, we have reviewed the model of third sound propagation in saturated films of ^{4}He. The experimental system used to study third sound in films from 1.6 K to the λ point has been described. The measurements were used to further understand the depletion of the superfluid density of the film. These results indicate that the model of third sound propagation may be improved by including the anisotropy of the superfluid density as predicted in [56]. Depletion of the superfluid density is well described by the model presented in Appendix B at low temperature and near the λ point. A possible explanation of the lack of depletion in the intermediate temperature range is presented. In order to progress with the explanation, a reformulation of third sound in terms of an anisotropic superfluid density is necessary.

The measurements of third sound attenuation are consistent with previous measurements in thick films [6, 5, 49]. In this experiment, attenuation was mea-

sured over a larger temperature range than previously. Beyond the range of previous measurements, a peak in the attenuation was discovered at 2.134 K for all of the films studied. In order to understand this peak, we explored the models of attenuation in terms of the thermohydrodynamics and vortex-unbinding to see if they could account for the peak. Neither model predicts a peak in the attenuation at that temperature. In Appendix C, we develop a model of the boundary transmission of third sound. This model yields a slight increase of 10 percent in the attenuation of third sound. None of the models discussed can account for the peak in attenuation. Interestingly, this new result may also be explained in terms of the anisotropy in the superfluid density.

Finally, we use the cutoff temperature and speed of third sound in the films to understand the KT transition. Both the loss of the amplitude and the phase signals are used to identify the KT transition in the films. We find that our measurements are consistent with the KT theory and previous measurements in thick films. As well, in the context of finite size scaling, our results are consistent with previous measurements in thick films, but disagree with Monte Carlo simulations and measurements in thin films. In the next chapter, the temperature where the KT transition occurs relative to the critical Casimir effect will be identified.

CHAPTER 3

Critical Casimir Effect

Saturated superfluid ^{4}He films are well suited for studying the critical Casimir effect. In the vicinity of the λ point, the finite thickness of the film imposes a constraint on the magnitude of the coherence length. This results in a contribution to the free energy difference between the film and the bulk from the critical Casimir effect, Eq. 1.8. Accordingly, equation (Eq. 1.7) relating the film thickness to the height above the bulk must be modified to include this term. The expression relating film thickness to the height, in the vicinity of the λ point, becomes

$$\frac{\gamma_0}{d^3}(1+\frac{d}{d_{1/2}})^{-1}+\frac{Vk_BT_c}{d^3}\vartheta(d/\xi)=m_{He}gh \tag{3.1}$$

In the case of ^{4}He, this will result in film thinning[22, 11]. By measuring the resulting film thinning, the scaling function, $\vartheta(d/\xi)$ can be quantified. To date, two systematic experimental studies[58, 10, 11][1] have been conducted prior to our investigation. In addition to experimental studies, theoretical calculations and more recently, Monte Carlo simulations can be conducted of the critical Casimir effect[22, 60, 14, 12, 9, 61] in the context of superfluid ^{4}He.

In this Chapter, we will review the previous work; both experimental and theoretical. Follow the review, the experimental techniques used to measuring the critical film thinning will be presented. The results will then be presented and discussed.

[1] The first experimental signature of the effect was observed in 1989, it is described in Ref. [59]

3.1 Theoretical Calculations and Simulations

Figure 3.1 taken from Ref. [9] summarizes much of the theoretical and experimental work for the critical Casimir effect in ^{4}He films. To simplify the presentation, we will adopt the convention used in Ref. [9] for the form of the scaling variable. We will use $x = l^{1/\nu} = t(d/\xi_+)^{1/\nu}$ with ξ_+=1.432 Å [27] for the scaling variable. This choice will simply comparisons between different results.

Initial calculations of the critical Casimir effect were made through field theoretical techniques, unfortunately, these techniques are limited to temperatures above T_λ [22]. Later on, mean field theoretical techniques were developed to study the effect[12, 13]. By this time, experimental measurements of the effect had been made[10, 11] and the agreement with the MFT results was only qualitative. The MFT results are plotted in Fig. 3.1 as a dashed dotted blue line and labeled 'MFT'.

In 2007, A. Hucht developed a Monte Carlo simulation technique for studying the critical Casimir effect which agrees very well with the experimental results [14]. This result is plotted in Fig. 3.1 as a dashed black line. This simulation is a generic simulation for the XY universality class and is not specific to superfliud ^{4}He. Thus, it does include the Goldstone modes mentioned earlier in Section 1.4. The dotted traces are the different results from Ref. [9] using a MC technique based on Ref. [14]. As can be seen, the agreement with Ref. [14] looks reasonable, though there is a considerable spread of the data.

The grey bar in the figure represents the KT transition in superfluid ^{4}He calculated from MC simulations in Ref. [15]. Their result is that $x_{KT} = -7.64(15)$ this value agrees well with previous measurements on unsaturated films far from T_λ, see Table 3.1. It will be seen, that our value for x_{KT} does not agree with the value from MC simulations. This will be discussed in Section 3.4.

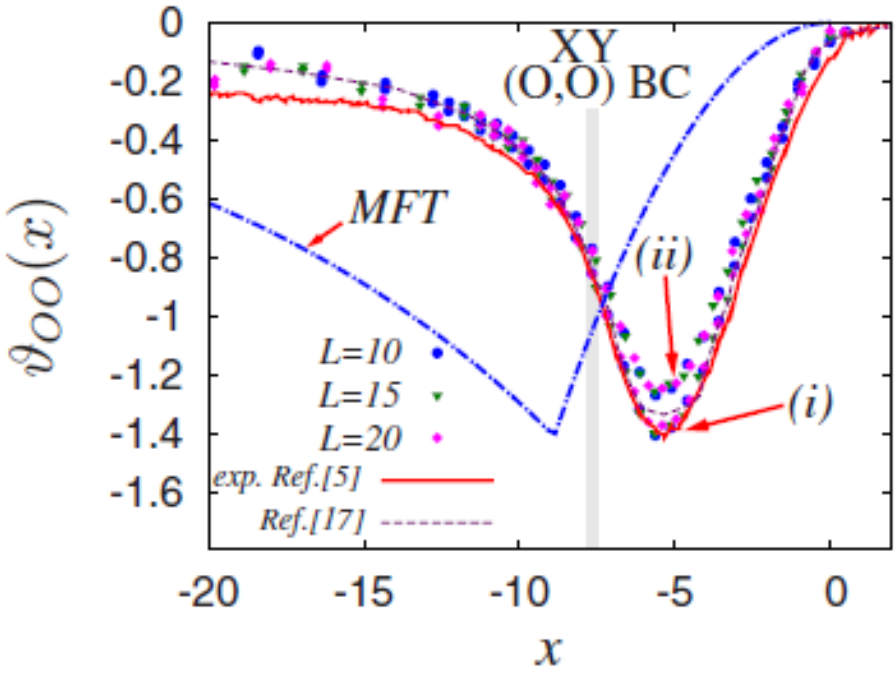

Figure 3.1: Figure 4 from Reference [9]. This figure summarizes much of the theoretical and experimental result for the critical Casimir effect in ^{4}He films. The red trace is the experimental results from Refs. [10] and [11]. The MFT trace is the Mean Field Theory results from Refs. [12] and [13]. The dotted black line is the Monte Carlo results from Ref. [14]. And the dotted series are MC results from Ref. [9]. The grey bar at x=-7.64(15) is the location of the KT transition as calculated by Mote Carlo siimulations in Ref. [15].

3.2 Previous Measurements

Figure 3.2 displays the results of the first systematic measurement of the critical Casimir effect in ^{4}He films near T_λ. To measure the film thickness versus temperature, they use a capacitance bridge technique. By measuring the change of capacitance between electrodes, they measure the film thickness of the ^{4}He film on the substrates which also act as electrodes for the capacitance bridge. For this experiment, a stack of six copper disks forms five capacitors. From the bottom of the cell to the top, they are labels 1 through 5. Accordingly, capacitor 1 should have the thickest film and capacitor 5 would have the thinnest film. Their results for the film thickness disagree when calculated from the change in capacitance versus calculating the film thickness from the height, Eq. 1.7. The disagreement varies from 10 percent for Cap. 5 to 100 percent for Cap. 3. As well, it can be seen from the scaling plot in Fig. 3.2 that the results do not exhibit data collapse. The authors speculated that the lack of data collapse could be related to the discrepancy in the film thickness. They note that their copper substrates have visible scratches and speculate that capillary filling of the rough surface could lead to an effective film thickness enhancement.

The data in Ref. [10] was taken by allowing the cell temperature to drift through the λ point by stepping the temperature of a thermal stage. The drift rates varied from 200 μK/hr to 7 mK/hr. At the time, the only available theoretical work to compare with were the field theoretical calculations above T_λ, Ref. [16]. In the lower plot of Figure 3.2, they compare their measurements with the prediction of Ref. [16] and the agreement looks reasonable. Although, there is a large spread in their experimental data.

In Figure 3.3, the results from the second experimental measurement of the critical Casimir effect in ^{4}He films is displayed. In this experiment, N-doped silicon substrates are used. This choice of substrate mitigates the issue of surface

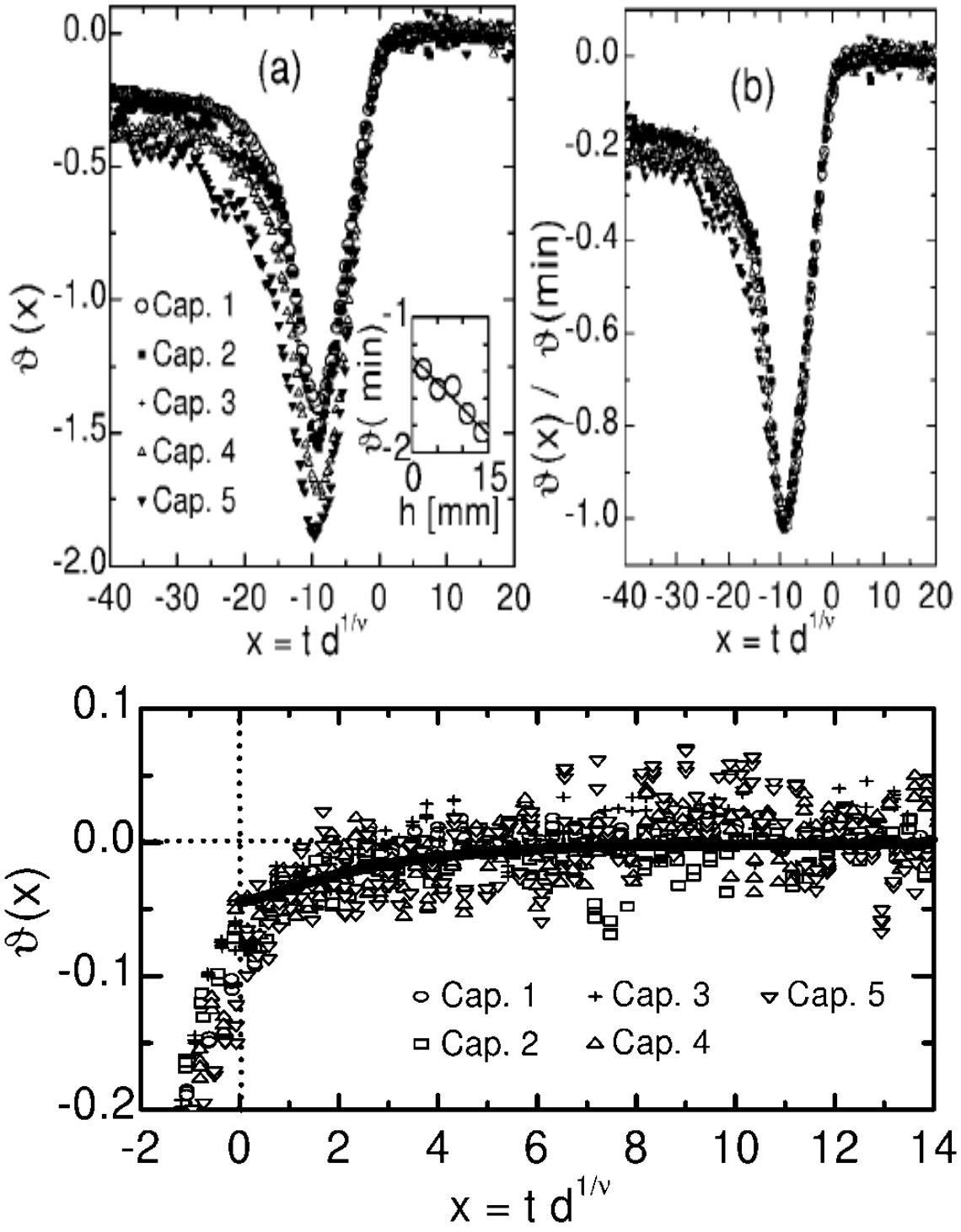

Figure 3.2: Figures 3 and 5 from Reference [10]. The upper left plot displays the scaling function versus the scaling variable. The upper right plot displays a normalized plot. The lower plot displays the scaling function results and a solid curve from a theoretical prediction in Ref. [16]. Notice that the data does not collapse.

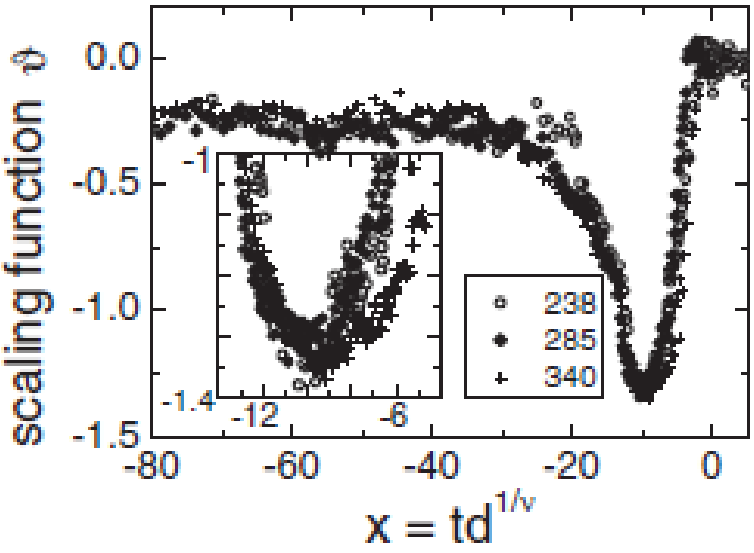

Figure 3.3: Figure 4 from Reference [11]. This is a plot of their main experimental result, the scaling function versus the scaling variable. In this experiment the results do exhibit data collapse. The legend displays the film thickness in Å for each data set.

roughness since the substrates are smooth to the atomic scale. The silicon is doped so that it will retain electrical conductivity at low temperature. They utilize a capacitance bridge technique to measure the film thickness. As can be seen in Figure 3.3, the results of this experiment do exhibit data collapse. Interestingly, they do not address how their data compares with the field theoretical calculations [16] of the critical Casimir effect above T_λ. The data from this experiment seems to display different behavior above T_λ from the data in Fig. 3.2. The data set for the 285 Å film seems to have a peak just below T_λ. The data for the 340 Å film, the thickest film for this experiment, is cut-off at T_λ. With this experiment, the sweep rates varied from 40 μK/hr to 300 μK/hr. Interestingly, they mention that gap filling was a major experimental challenge of their work. And that it could be resolved by conducting repeated slow sweeps through the λ point.

3.3 The Capacitance Bridge

In this section, we will describe the experimental techniques specific for the study of the critical Casimir effect. As noted previously, the general experimental set-up is reviewed in Appendix A. Through proper design and fabrication, capacitance bridges are able to measure extremely small changes of the dielectric constant of a material in the measurement side of the bridge. Reference [55] contains an introductory review of capacitance bridge technique.

We measure the capacitance between the main electrode and a specific quadrant or collection of quadrants in order to measure the film thickness, see Fig. 3.4 for schematics of the electrode assembly. The capacitance is measured with a ratio transformer bridge using an identical substrate assembly mounted on the exterior of the cell for a reference capacitor, see Fig. A.5. Our design is based on previous measurements of helium films [62, 10, 11].

In order to limit the possibility of capillary filling of the small gap (60 μm)

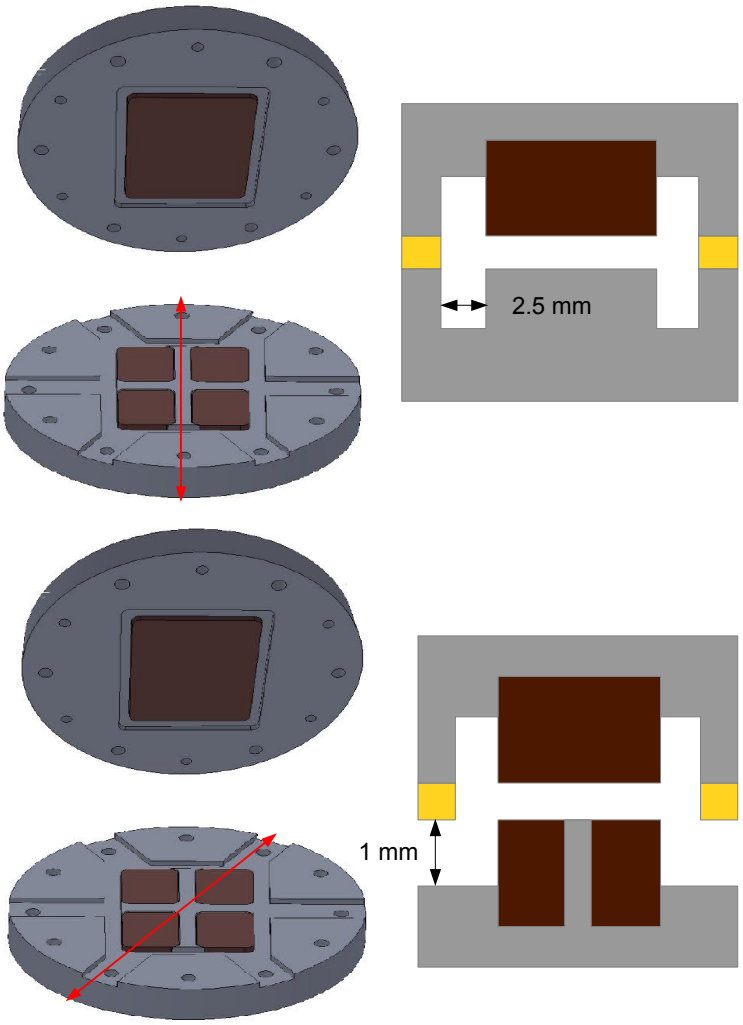

Figure 3.4: Schematics of the electrode assembly, exploded views on the left side. The red arrows indicate the direction for the cross-sectional views on the right. Sections in grey indicate the electrode supports. The brown sections label the electrodes which define the capacitor. The yellow indicates the 60 μm thick Kapton spacer.

between the electrodes, we developed a novel substrate assembly design. The channels around the electrodes isolate the measurement substrates from the mechanical assembly used to define the gap. Thus, if there is a wetting event in the mechanical assembly, it is unlikely to fill the substrate gap. In the experiment by Ganshin et. al. [11], they had considerable issues with the gap filling. In our experiment, the gap did not fill even with the thickest film studied. With the split quadrant design, this experiment would be sensitive to partial gap fills as well. During the experimental run, no filling events were found.

As noted in the previous experiments[10, 11], surface roughness is a important design consideration for film measurements. For the surface preparation of the substrates used in this experiment, we utilized diamond turning to achieve surface roughness on the level of 10 nm[2]. The substrate preparation and further details of the experimental cell are contained in Chapter 2, Section 2.2.1. Within the gap formed by the substrates, there is ^{4}He vapor in addition to the helium film adsorbed on the substrate surfaces. See Fig. 3.5 for a diagram of the space.

In order to extract the film thickness from the capacitance measurement, the contribution to the gap capacitance from the vapor must be subtracted out from the signal. As seen in Fig. 3.6, the change in the capacitance with temperature is dominated by the changing density and thus the dielectric constant of the vapor. Just below T_λ, a dip in the capacitance is observed. This dip corresponds to a thinning of the film due to the critical Casimir effect, see Section 1.4.

The film thickness value is extracted from the capacitance using the same technique as in Ref. [11]. For our experiment we make measurements on four different film thicknesses; 270, 300, 344, and 480 Å. The capacitance of the gap can be expressed in terms of three contributions; the empty cell capacitance, the film contribution, and the vapor contribution. The dielectric constant of the vapor can be calculated from the Clausius-Mossotti equation by calculating the

[2]The Diamond turning was performed by KAF Manufacturing, Inc.

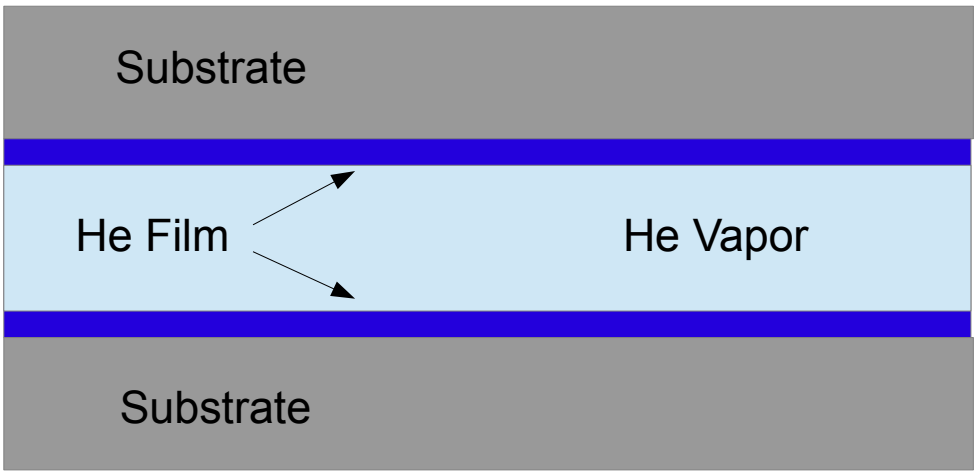

Figure 3.5: Sketch of capacitor gap displaying the film and vapor geometry.

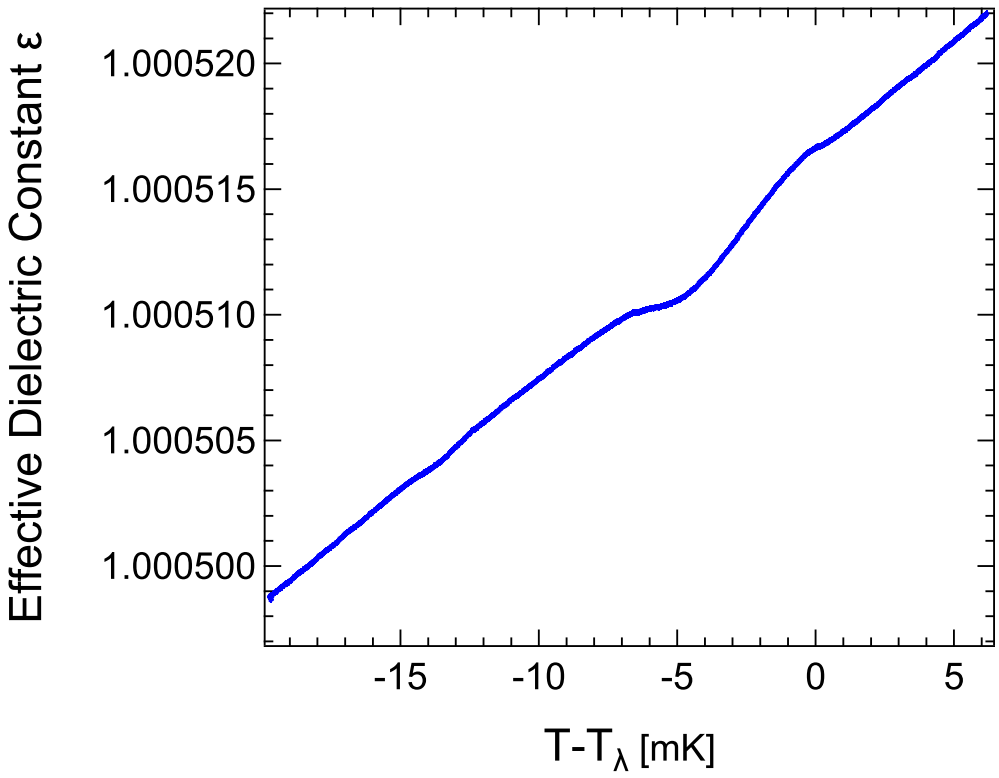

Figure 3.6: Data from the capacitance bridge for the 344 Å film. The effective dielectric constant is plotted versus the temperature from T_λ.

vapor density from the pressure using the second virial coefficient. The empty cell capacitance is measured prior to the cell fill. Within our experimental uncertainty, it is constant over the temperature range of the measurements. The dielectric constant of the film is taken to be constant over the range of measurement. The film thickness can be solved for in terms of the other quantities. The resultant expression is

$$d = \frac{G}{2}\left(\frac{1}{\epsilon_{vapor}} - \frac{1}{\epsilon(T)}\right) / \left(\frac{1}{\epsilon_{vapor}} - \frac{1}{\epsilon_{film}}\right) \tag{3.2}$$

where G is the gap size, 60 μm for our experiment. The effective dielectric constant, $\epsilon = C(T)/C_0$ is the ratio of the measured capacitance from bridge to the empty cell capacitance. As found in Ref. [11], we have a small temperature dependence which must be factored out. Following their analysis, we conjecture that this temperature dependence is due to having the electrodes potted in the holder. We find the correction is of the same order of magnitude as in Ref. [11].

The constant film thickness value is measured by performing a third sound frequency sweep near the base temperature. This method is discussed in Section 2.2.3. There are two alternate ways of establishing the film thickness. One is through estimating the height of the substrate above the surface of the bulk ^{4}He in the cell. This is done by estimating the amount of ^{4}He introduced into the cell during dosing. The other technique is to extract the film thickness change from the change in capacitance of the electrodes using Eq. 3.2. The two alternate ways are more subject to systematic error than the third sound technique. As will be discussed in a later section, Section 3.4.2, there is some question as to what is the actual equilibrium value of the film thickness far from the critical region.

The uncertainty in our film thickness measurement is limited by the stability of the ratio transformer and the ^{4}He film itself. The ratio transformer has a temperature stability of $\frac{\delta R}{\delta T}$=1 ppm K^{-1}. We regulate the temperature of the

Source	ϑ_{min}	x_{min}
Monte Carlo [14, 9]	-1.35(3)/1.396(6)	-5.3(1)/5.43(2)
Measurements [11]	-1.30(3)	-5.7(5)
This Work	-1.2(1)	-6.0(5)

Table 3.1: Compilation of results for the Critical Casimir Effect in ^{4}He films. The values for the Monte Carlo simulations is the average from the results from the cited sources.

ratio transformer by placing it in an insulating box. In this way we are able to maintain a stability of .1 K for the ratio transformer for a time scale on the order of days. Near the λ point, the thermomechanical effect is maximum [23] thus the system is most sensitive to temperature gradients within the cell. A temperature gradient across the substrate will lead to a corresponding pressure gradient across the substrate. This pressure gradient will induce a film thickness change. In the vicinity of T_λ, a 1 μK temperature gradient will change the film thickness by 1 Å. In order to properly measure critical effect, the system must be thermally swept at a very slow rate and must be in good thermal equilibrium with the bath. To study the critical Casimir Effect, we use a sweep rate of 400 μK/hr. We find this rate is sufficiently slow to measure the dip on film thickness in agreement with previous measurements[10, 11]. For films thicker than 300 Å, the lower surface of the substrate assembly is submerged in bulk ^{4}He. This in conjunction with the fact that we are using OFHC copper for our assembly provides the system with a very good thermal system for studying effects in the vicinity of the λ point. Overall, our uncertainty in film thickness changes is 0.5 Å. Whereas the uncertainty in the total film thickness is about 10 Å.

3.4 The Critical Casimir Effect

Our results for scaling and the dip agree well with previous measurements and simulations, see Table 3.1. In Figure 3.7, we display the measured film thickness change. Our results agree generally with those found by Gashin et al. [11]. We find that there is a film offset below T_λ for all of our films expect for the thickest one, 480 Å. This discrepancy may be explained by the film thickness dependence of the surface modes as calculated in [18], thicker films should have a smaller offset. For a 500 Å film, it will be less than one Å. As well, our measurements for ϑ_{min} and x_{min} agree reasonably well with previous results [14, 11, 9]. When plotting the data for the films measured here on Fig 21 of [17], there is very good agreement, see Figure 3.8. Our data confirms that the critical Casimir minimum occurs at the same value of the scaling variable as the specific heat maximum, an interesting result which for which there is no theoretical explanation as of yet.

We do find a somewhat smaller value for ϑ_{min} than was found in previous measurements. This may be due to surface roughness of the substrates in previous measurements. Lowering the surface roughness of the substrate is critical for properly measuring the dip as has been revealed by previously. The fact that we see a smaller dip indicates that surface roughness is not an issue with our measurements. The dominate source of uncertainty for our measurements of ϑ_{min} and x_{min} is the uncertainty in the equilibrium film thickness.

3.4.1 KT Transition versus the Casimir Dip

In addition to measurements of the film thickness, we are able to measure the superfluid density in the film through measuring the third sound response of the film, see Section 2.3.4. Through measuring the superfluid density we are able to find the KT transition in the films[33]. We find with our measurements that the KT transition in the film occurs at the beginning of the dip, x_{KT}=-11.1(4).

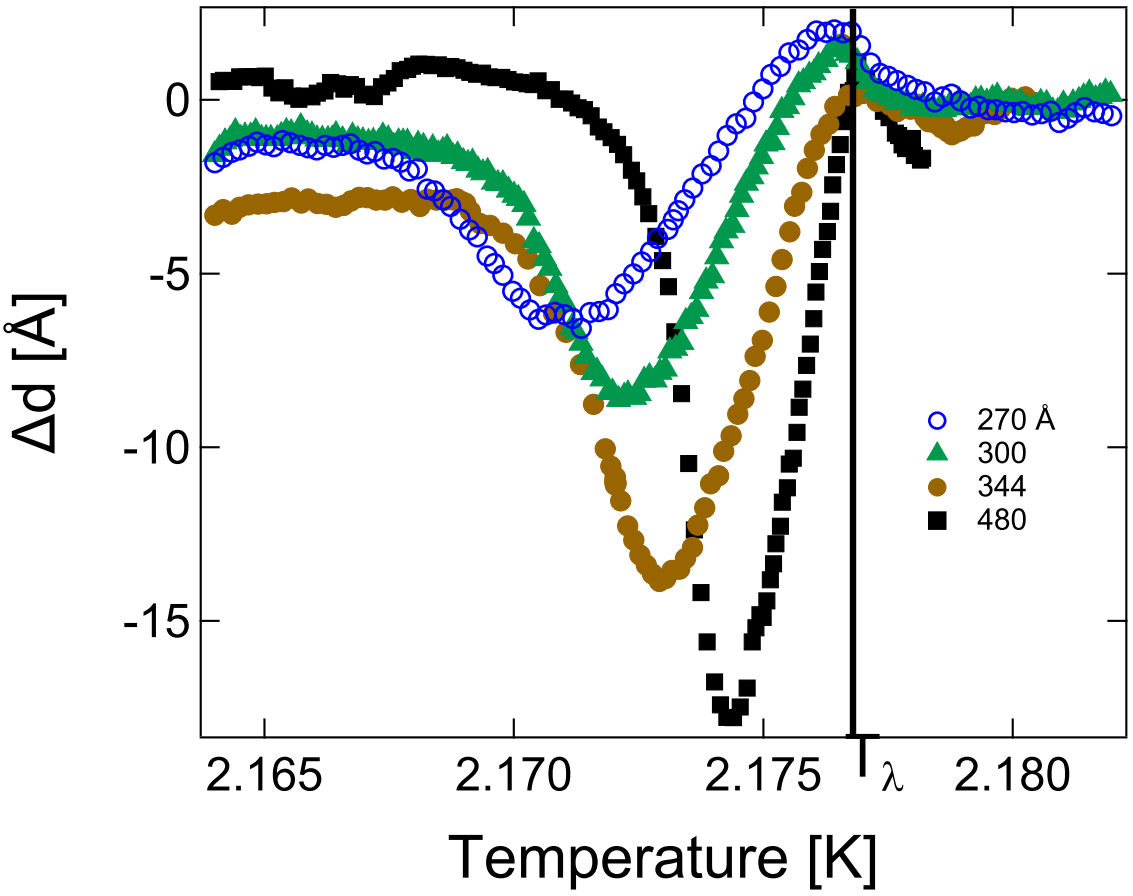

Figure 3.7: Measurements of the thickness change in Angstroms for the four films studied. The film thickness above T_λ for each film is indicated in the legend.

Monte Carlo simulations place the KT transition between the beginning the dip and the dip minimum at x_{KT}=-7.64(15) [9, 15]. Whereas mean field considerations indicate that the KT transition should occur in the vicinity of the dip minimum [12]. Our result indicates that the majority of the Casimir effect occurs when the film is in the normal phase at long length scales. At short length scales and finite frequency, the superfluid phase is present in the film [34]. This result may aid in developing a clearer understanding of what underlies the critical Casimir effect in ^{4}He films. Interestingly, Vortex Loop calculations of the critical Casimir effect predict that the film will undergo the KT transition at the beginning of the dip [60]. As well, our location of the KT transition relative to the dip minimum agrees well with a previous measurement [11].

3.4.2 Film Step at the λ point

For the data in Figures 3.7 and 3.9, the temperature is swept through the λ point at a rate of 400 μK/hr. At this sweep rate there is a noticeable rise in the film thickness at T_λ. In previous measurements, this rise is also discernible [11, 19]. When the temperature is swept through the λ point at a much lower rate (5 μK/hr), this rise becomes a step in film thickness, see figure 3.10 with the film being thicker above T_λ. This result has not been reported in previous measurements nor in simulations of critical effects in the vicinity of the λ point. The magnitude of the step increases with increasing film thickness. When the step size is used to calculate the change in the Van der Waals attraction at the surface of the film it is found that for all of the film, the energy is approximately 1 μK per atom. Since the ^{4}He in the film is well away from it's transition temperature, T_{KT}, the source of the changing free energy should lie in the bulk. In essence, the film is acting as a probe of the bulk free energy. We can start from the expression for the equilibrium film thickness, Eq. 1.7, and add a constant term for the free energy change of the bulk. This yields;

$$\frac{\gamma_0}{d^3}(1+\frac{d}{d_{1/2}})^{-1}+\Delta F = m_{He}gh \tag{3.3}$$

Taking the differential of this, we find that;

$$\frac{\Delta d}{d} = \frac{\Delta F}{U_{\text{vdw}}} \tag{3.4}$$

In Figure 3.11, we plot the ratio of the film thickness change to the film thickness and compare that to a plot of a constant 1 μK energy versus the Van der Waals energy as a function of film thickness. From the plot we can see that the measurements indicate that the step in film thickness at the λ point corresponds to a constant change in the free energy of the bulk.

The fact that the shift is constant in energy, i.e. it scales with film thickness is another indicator that the source of the change lies with the bulk. From our measurement of the step height, we can estimate the change in the Van der Waals energy of the film at the λ transition. For the different films we measured, we found the same value of the change in the Van der Waals energy per atom, see Fig. 3.11. The energy change is 1 μK per atom. We can interpret this as the energy associated with the transition per atom in the bulk. We can multiply this energy per atom by the number of atoms in the bulk to get an idea of the energy change in the bulk at the transition.

$$\Delta U_{bulk} = 1\frac{\mu K}{atom}k_B N_A \frac{.145g}{4g} = 1\frac{erg}{cc} \tag{3.5}$$

The energy change in the bulk is expected to be approximate 1 erg for a 1 cc bulk sample from this analysis. As a first step in understanding this new effect, we can look to the second sound modes. In the film, the motion of the normal component will be suppressed at low frequency through it's viscosity and proximity to a surface. This effect is characterized by the viscous penetration depth [44, 63], see Section 2.1 for a description of the viscous penetration depth.

For a 300 Åfilm, the viscous penetration depth is approximately 50 μm for a 100 Hz oscillation. When the oscillation frequency is 6 MHz, the viscous penetration depth will be about 300 Å. The spectrum of thermally excited second in the film will be either be reduced or entirely excluded relative to the bulk owing to the viscous penetration depth. This should lead to a free energy difference between the film and the bulk. The Debye model can be used to develop an estimate of the free energy from second sound in the bulk [25]. To use the Debye model, we require an expression for c_2 and a cut-off frequency for second sound as functions of temperature. In the hydrodynamic regime, where ξ is much smaller than the wavelength of second sound excitation, there is ample data to generate those expressions.

In Appendix D, we attempt to use data[2, 64] from the hydrodynamic regime to get a result from the Debye model for the bulk free energy. The result is not physically meaningful. Near the lambda transition, where ξ diverges, thermally excited second sound enters a critical regime where $q\xi \gg 1$, q is the wavenumber of the characteristic excitation[65]. In this regime, there is not a good understanding of the dynamics of thermal second sound. The experimental results from light scattering [66] are not consistent with the results of dynamic critical phenomena. The data shows that, at high frequency, c_2 does not go to zero. Our results provide new information for developing our understanding of thermal second sound in the vicinity of the lambda transition.

From the energy of 1 μK per atom, we can estimate the upper limit of the second sound fluctuations in the bulk at the λ point by using the data of Ref. [66] to estimate $c_2(T_\lambda)$. Through this analysis, the upper bound for the frequency of the modes is 10 MHz. This result could provide a point for future experiments on the onset of thermal second sound in superfluid helium. These fluctuations are distinct from those discussed in Ref. [18, 12] in that the second sound excitations we are considering are non-universal because of the changing speed of the second

sound and a viscous cut-off.

For the slow sweeps, the temperature is swept at 5 μ K/hr, we find that the capacitance take approximately 12 -15 hours to equilibrate to a final value at T_λ. There is no know vapor or bulk anomaly which this step could correspond to. The step is reproducible when swept from above or below the λ point. As well, the same magnitude of step is found when different quadrants in our cell are used to measure the step. This excludes capillary filling from being the source of the step. The hold time of our cryostat is 7 to 8 days. So, we are able to sweep through the step anomaly without having to perturb the system with a bath transfer. Once a transfer to the bath is performed, the capacitance of the system is perturbed and takes approximately one day to recover the equilibrium value. We speculate that the reason for the long time scale for the film to come to equilibrium for the step is that the bulk He is connected to the film via a normal film. The He atoms in the vapor respond to the free energy difference between the film and the bulk through a concentration gradient. The equilibration time associate with the gradient is on the order of hours based on modeling the vapor as an ideal gas and computing the diffusion time. This calculation is reviewed in Appendix E.

3.5 Discussion

In summary, we have undertaken measurements of the critical Casimir effect and superfluid density in thick films of ^{4}He. We find that finite size scaling is valid and that our measurements agree with previous measurements and simulations. We locate the KT transition relative to the dip maximum and find that the KT transition in the film occurs at the beginning of the dip. Additionally, we find a step in film thickness which can be understood in terms of a new non-universal component to the critical Casimir effect. We attempt to develop a model to account for this new effect from the viscous suppression of second sound modes

in the film, see Appendix D. This new critical Casimir effect may provide insight for the question of thermal second sound in the vicinity of T_λ.

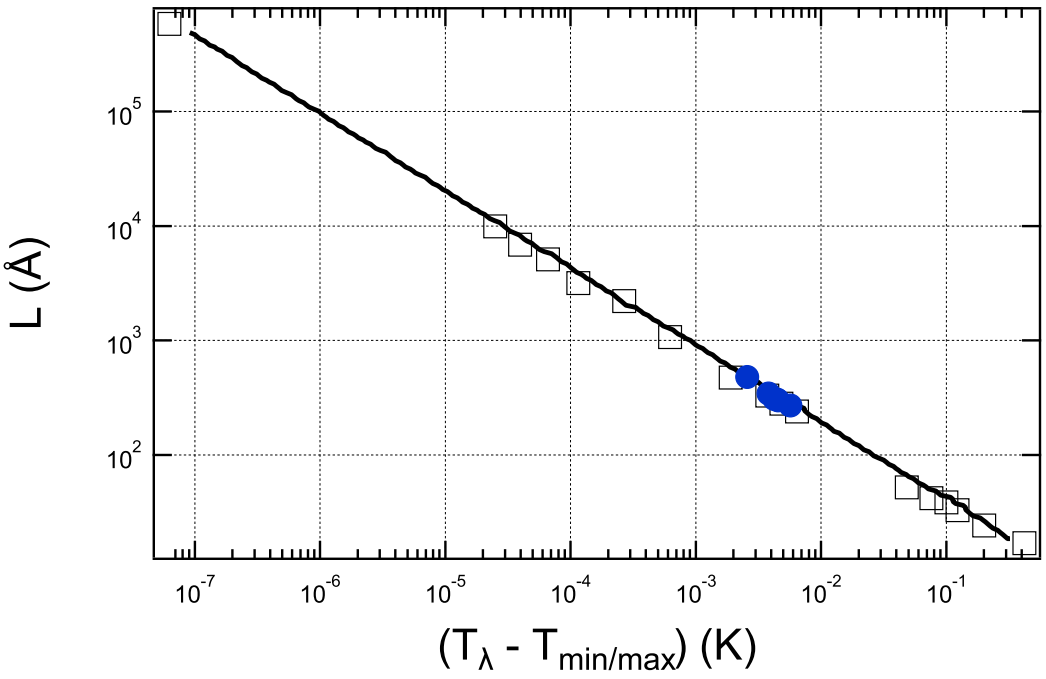

Figure 3.8: Plot of data from Figure 21 from [17] with our data plotted in solid.

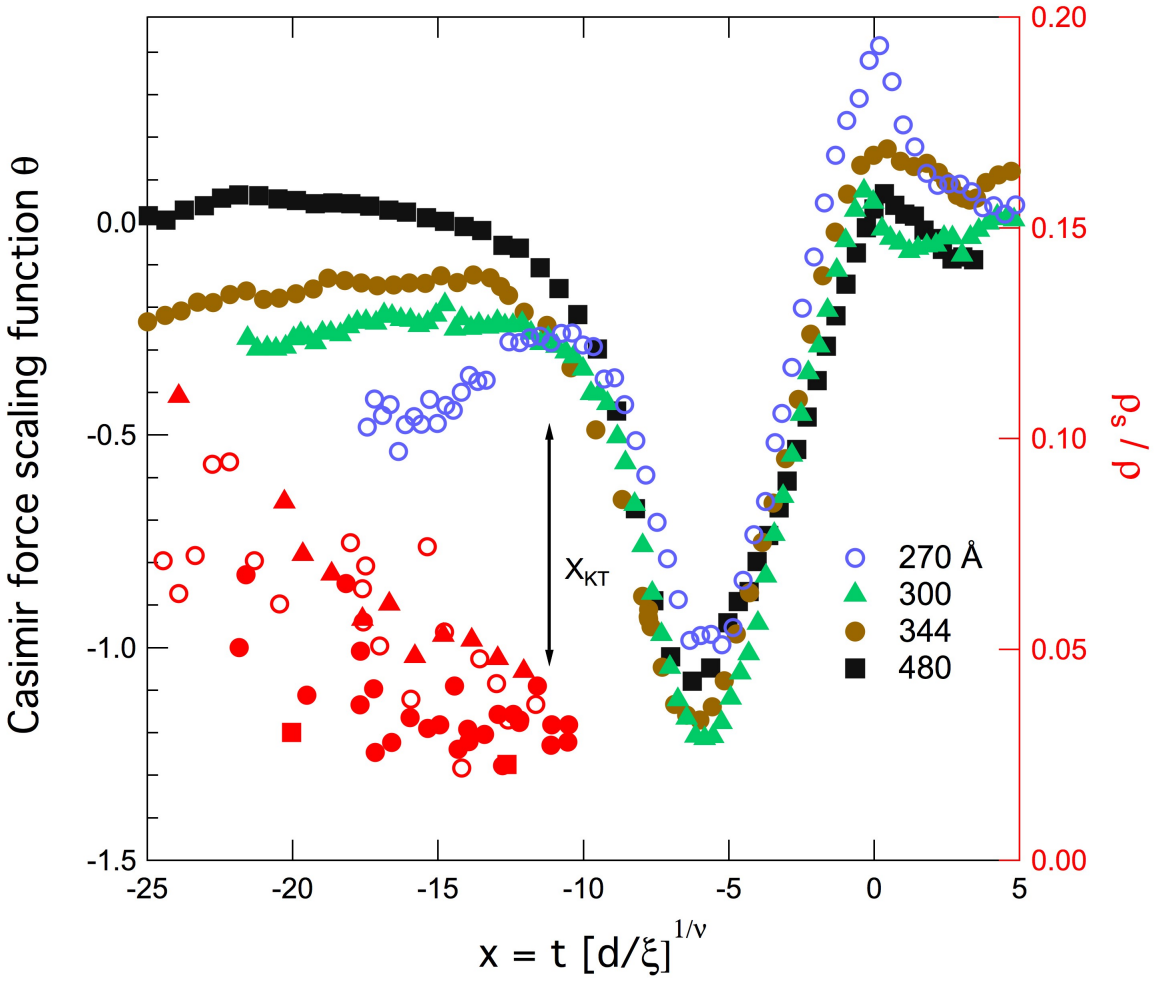

Figure 3.9: This is our result for the ciritcal Casimir effect and our measurements of the superfluid density. The traces in red are of the superfluid density. The location of the KT transition x_{KT}=-11.1(1) is indicated with an arrow.

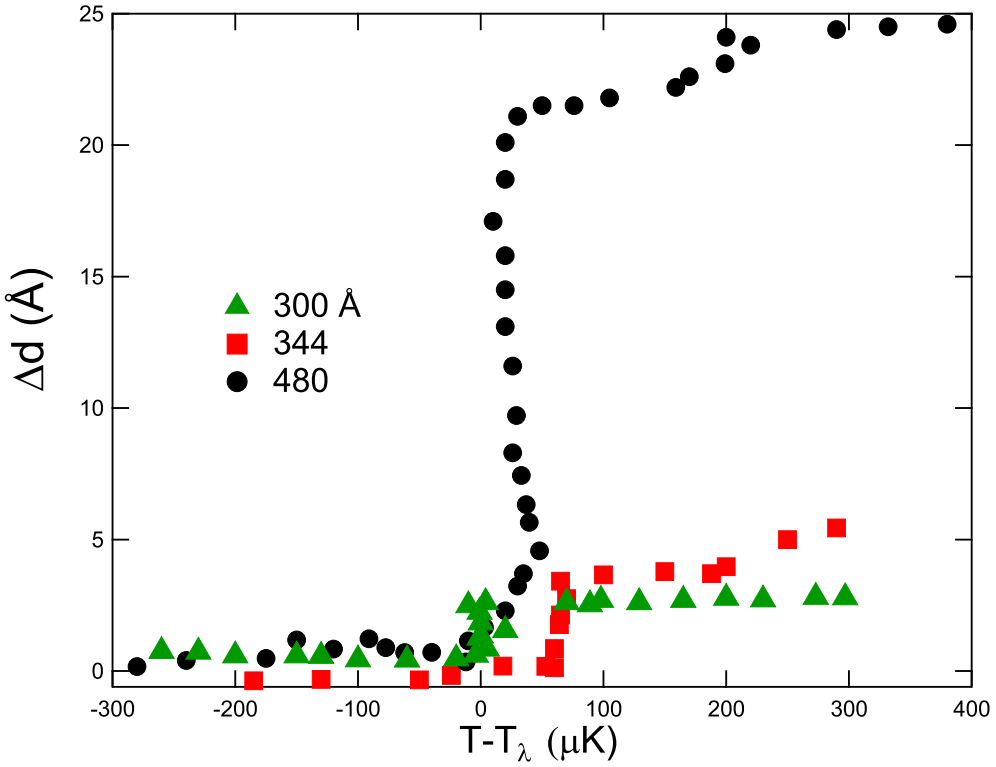

Figure 3.10: Results of slow sweeps across T_λ. The sweep rate is 5 μK/hr. The step is reproducable when swept from above or below.

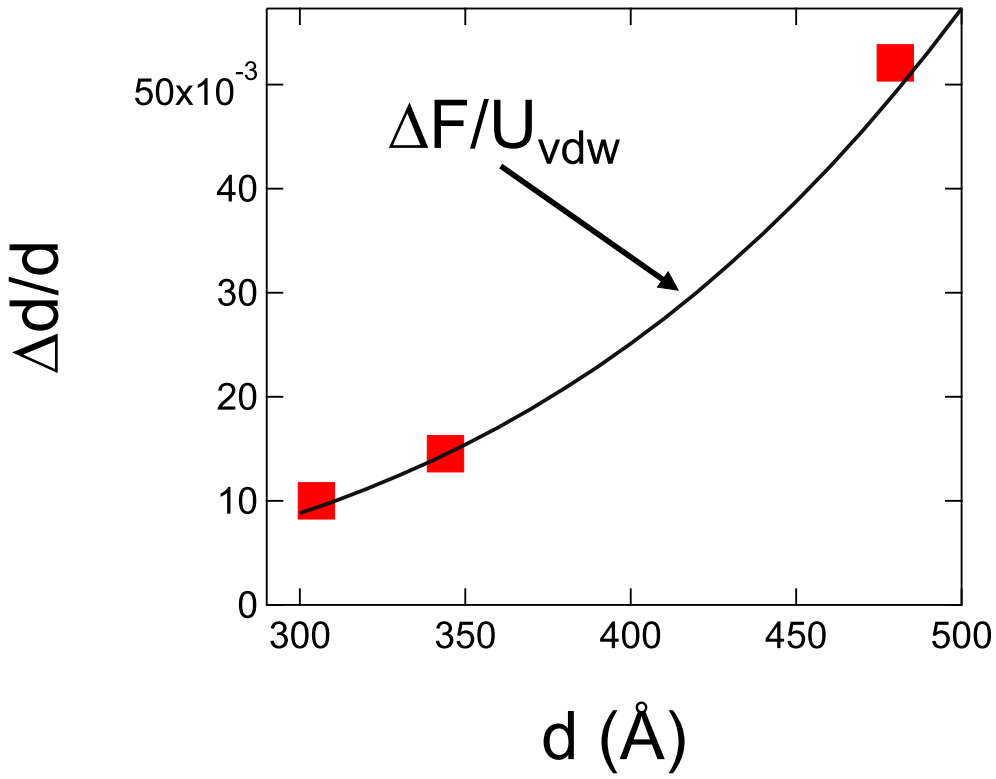

Figure 3.11: Plot of the ratio of the film thickness step to the film thickness versus the film thickness. The curve is the ratio of a fitting energy, ΔF, to the Van der Waals energy of the film. The fitting energy corresponds to 1 μK.

APPENDIX A

The Cryostat

In this appendix, the general experimental set-up and methods used for both the third sound and the critical Casimir effect measurements are described. For this experiment, a continuous flow 1 K pot cryostat on loan from the Jet Propulsion Laboratory was rebuilt, see Figure A.1 for a picture of the cryostat. For a basic review of 1 K pot cryostats, see Refs. [67, 55, 25]. A vacuum can attaches to the bottom of the 4 K flange and defines the volume for the experimental space of the system. The cryostat is inserted into a LN_2 jacketed research dewar supported by air springs to reduce vibrational sources of noise. The hold time of the ^{4}He bath is approximately 1 week. The hold time sets the limit for the time to perform measurements of an undisturbed system. This is a fundamental limitation for studying an undisturbed film. The thermal variations caused by the bath transfer can take up to a day to dampen out. In Figure A.2, a diagram of the interior space of the vacuum can is presented. In this Appendix, we will describe the major components of the cryostat. Connections to the components within the vacuum can are made through the 4 K flange via electrical and vacuum feedthroughs. The primary components within the vacuum can are the 1 K pot, thermal regulation stages, and the experimental cell. Each of these systems will be reviewed in the following sections.

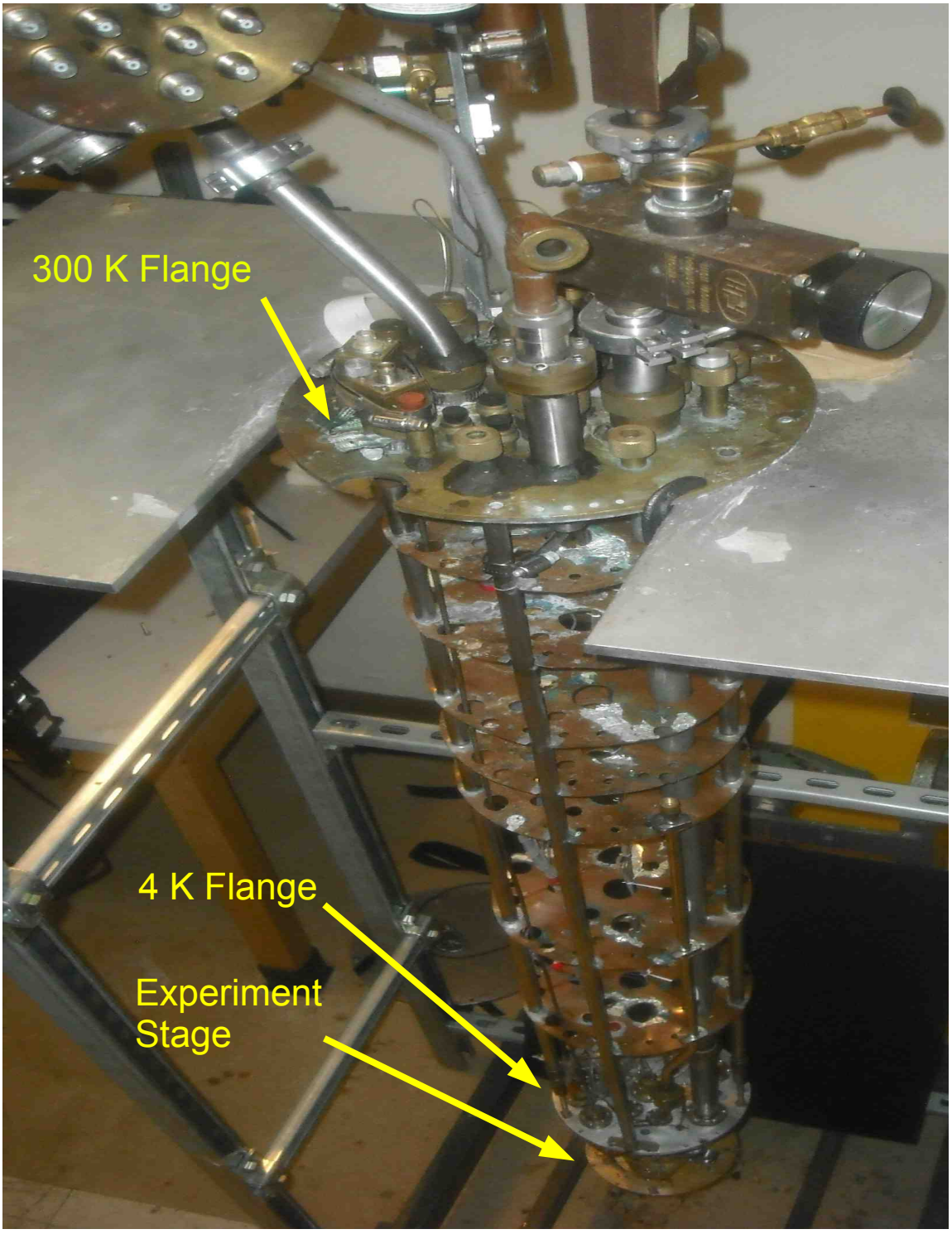

Figure A.1: Picture of the Cryostat. The various stages of the cryostat are labeled for reference.

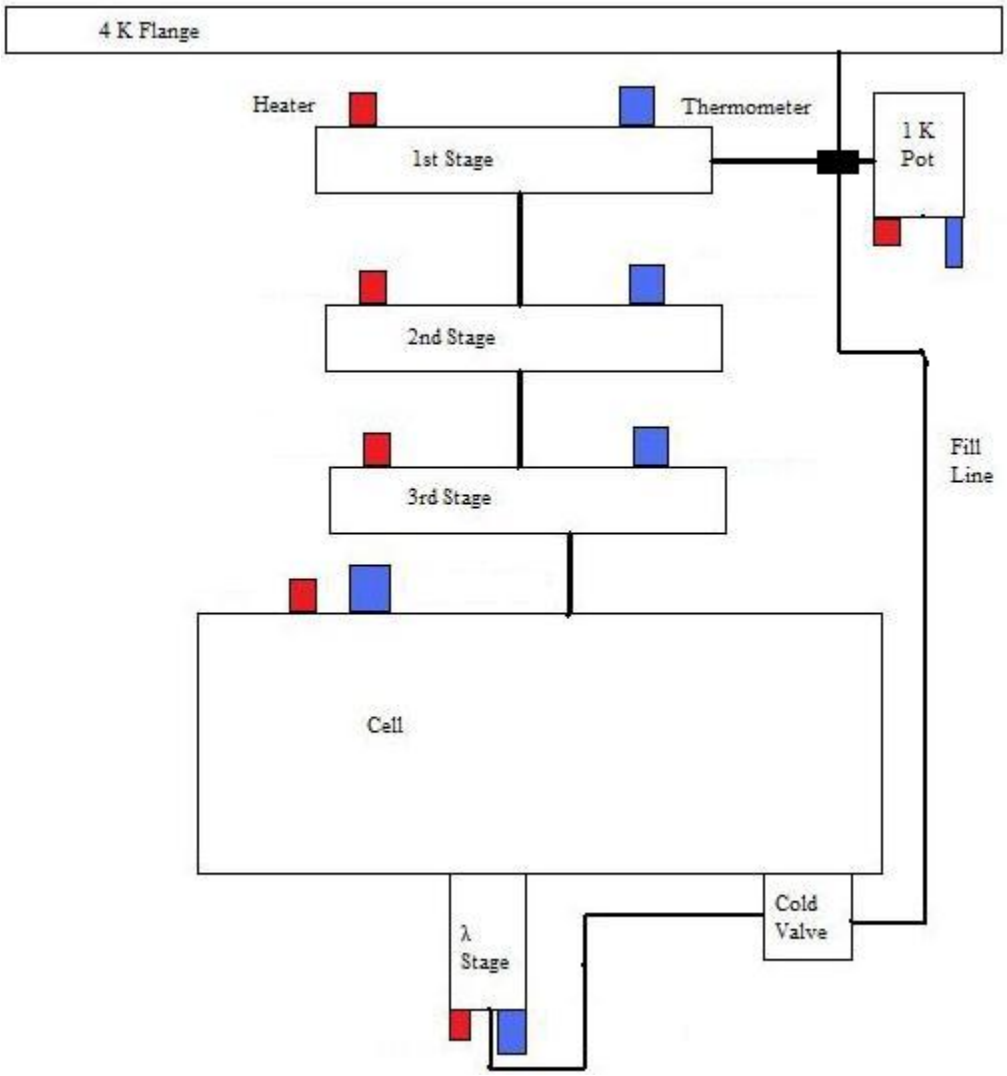

Figure A.2: Diagram of the experiment inside of the vacuum can. Heaters are indicated in red, thermometers are indicated with blue. The cold valve is indicated as being on the cell since it is thermally anchored to the cell. The purpose of this diagram is to map the intended thermal network. External heat loads are not indicated.

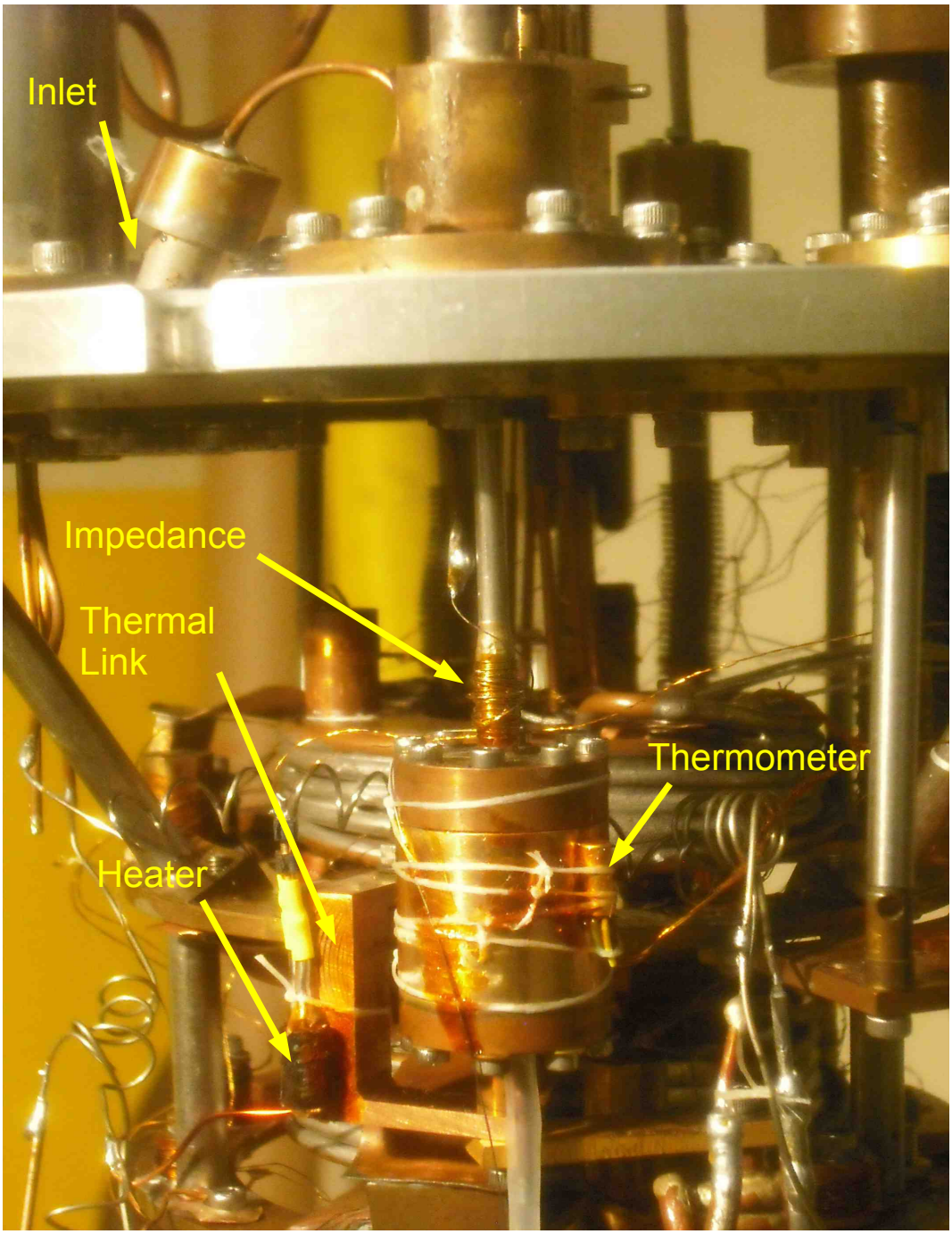

Figure A.3: Picture of the 1 K pot as mounted in the cryostat. Components of the pot are indicated in the figure. The impedance is a fine capillary tube. In the picture, most of the impedance is wrapped around the top of the pot. The mating surfaces of the pot are gold plated in order to minimize the thermal boundary resistance.

A.1 1 K Pot

The 1 K pot is the source of cooling power for this experiment. The 1 K pot system can be understood as composed of three elements; a pumping line to room temperature which connects to a pump, a volume to contain LHe, and a capillary line connecting the volume to the LHe bath space exterior to the vacuum can. The volume is often referred to as the 'pot'. The capillary line acts as a flow impedance to regulate the filling rate of the volume. The pressure differential across the impedance acts to siphon LHe in the pot. See Figure A.3 for a picture of the pot used for this experiment. The recipe detailed in [55] was used to construct (and troubleshoot) the 1 K pot system.

The base temperature and the ultimate cooling power of a 1 K pot are related to each other through the impedance of the fill line by an empirical relation which was first described by L.E. DeLong et al.[68]. This equation establishes the trade offs in 1 K pot design. Through tuning the magnitude of the impedance, the base temperature and the cooling power of the pot is determined. A higher impedance will result in a lower base temperature, but that is at the expense of cooling power and thus thermal equilibration times. The impedance of the pot line is adjusted to optimize the cryostat performance to the requirements of the experiment. The base temperature for our experimental run was approximately 1.5 K with a cooling power of a few mW. It is critical to thermally isolate the 1 K pot from external heat loads to maximize the available cooling power and attain the lowest base temperature. The 1 K pot is thermally isolated from the 4 K flange by using a thin walled stainless steel tube to mount the pot to its flange. The heat load from thermal radiation propagating though the pumping line is minimized by placing radiation baffles in the 1 K pot pumping line.

The 1 K pot is thermally anchored to the experimental cell through three thermal stages, see Figure A.2. The connection to the thermal stages is through a

link designed to maximize the thermal conductivity between the 1 K. The mating surfaces are gold plated and the thermal link (see Fig. A.3) is fabricated from OFHC copper.

A.2 Thermal Regulation

The remainder of our temperature regulation system is composed of three successive thermal stages between the pot and the experimental cell, see Figure A.4. Germanium resistance thermometers and resistive heaters are placed on each stage and the pot. Two sets of a thermometer and a heater are mounted on the cell. One set is on the cell body and the other set is on the λ stage, see Section A.3. Thermal connections are made between successive stages through high conductivity OFHC Copper wire of $\frac{1}{8}$ inch diameter. Copper washers are hard soldered to the ends of the wires, the assemblies are ultrasonically cleaned with acetone and then the mating surfaces are electroplated with gold. All of this is to ensure the highest thermal conductivity between successive stages to minimize thermal time constants and lower thermal resistance between stages [67]. Temperature was measured and controlled using PID temperature controllers [1].

For experimental runs, the three thermal stages were controlled with the PID temperature controllers and the experimental cell was not directly controlled. Approximately 1 mW was used to control the temperature of the system near T_λ. For our measurements near T_λ, above 2 K, we raise the base temperature of the pot by throttling the conductance of the pot pumping lime. This is done to limit the amount of heat that must be introduced to regulate the system temperature. In this way, we further minimize thermal gradients in the cell.

A generic calibration curve is used for all the thermometers except for the one mounted on the experimental cell. The cell thermometer is calibrated using the

[1] Neocera LTC-21

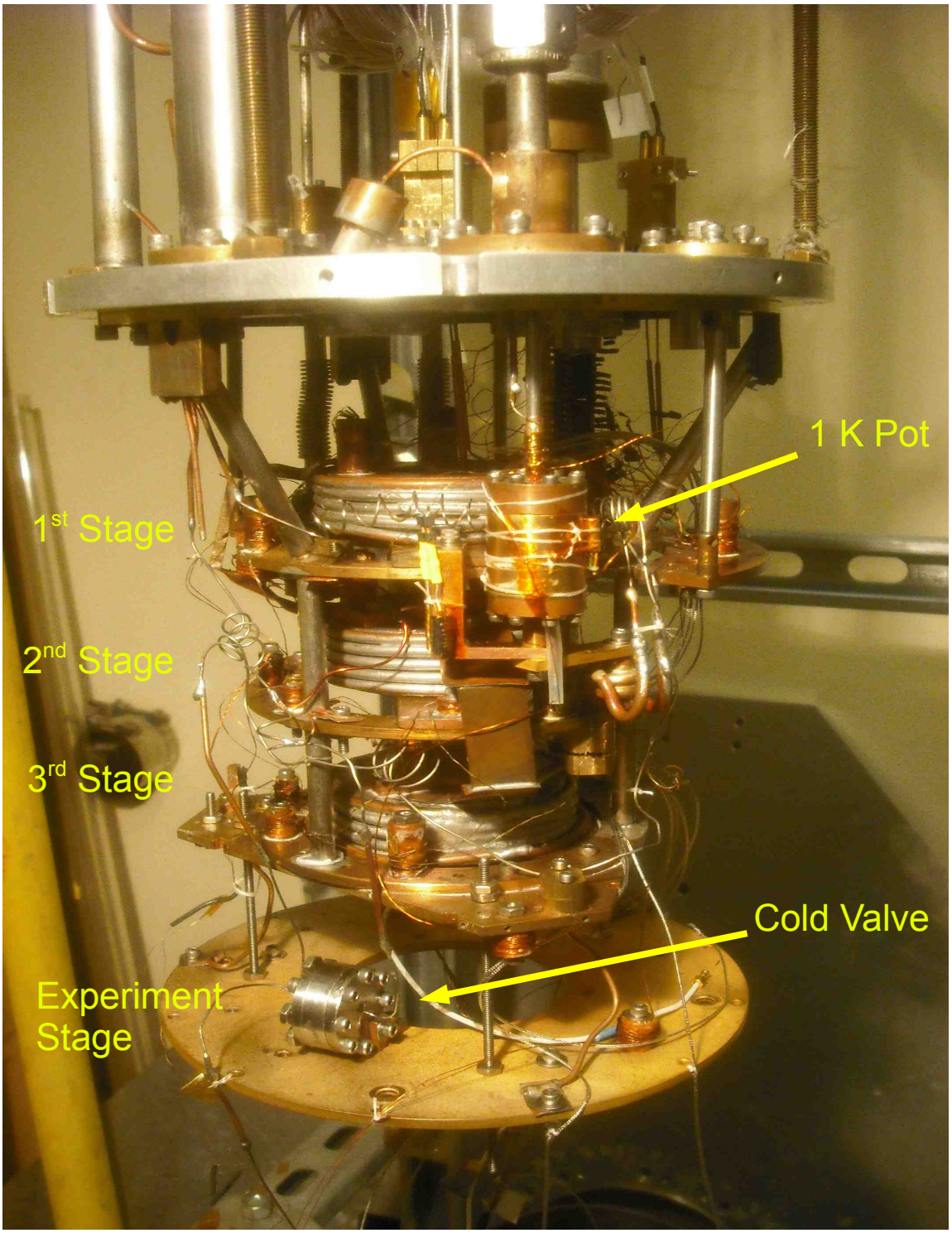

Figure A.4: Picture of the interior of the vacuum can. The various stages within, the 1 K pot, and the cold valve are labeled for reference. The experimental cell is bolted to the bottom the experimental stage.

^{4}He vapor pressure curve and the λ stage. The λ stage provides a measurement of T_λ, it will be described in the following section. The bulk of the data to calibrate the cell thermometer is from the vapor pressure curve calibration.

The vapor pressure calibration was performed by introducing enough helium to achieve a saturated vapor in the vacuum can in order to thermally short the thermometry to the bath. The bath was then pumped through a mechanical pressure regulator[2]. The regulator was used to throttle an impedance between the bath and the pumping line in order to regulate the pressure in the bath. In this way, the pressure in the bath was stepped through the λ point allowing the system to thermally equilibrate between pressure steps. The pressure in the bath was measured with a Baratron pressure gauge. This calibration was conducted at the end of the experimental run since it required the introduction of helium into the vacuum can space. In the next section, the experimental cell will be described.

A.3 The Experimental Cell

The experimental cell has four primary components; the electrode assembly, flange, body, and the reference capacitor assembly, see Figure A.5 for a picture of the cell. The cell is fabricated from oxygen free high conductivity copper for it's high thermal conductivity in the temperature range of interest [55, 67]. Thermal connections to the cell from the third stage are made in the same way as described in the previous section. Nested within the cell is the electrode assembly. The helium film is adsorbed onto all surfaces with the cell body, but measurements are only performed on the the film adsorbed on the opposing surfaces of the electrodes within the assembly, see Figure 3.4.

The electrode assembly is fashioned from oxygen free high conductivity copper for the superior thermal conductivity it provides. The bottom half of the electrode

[2]Precision Pressure Regulator Mark II, Del Monte Technical Associates

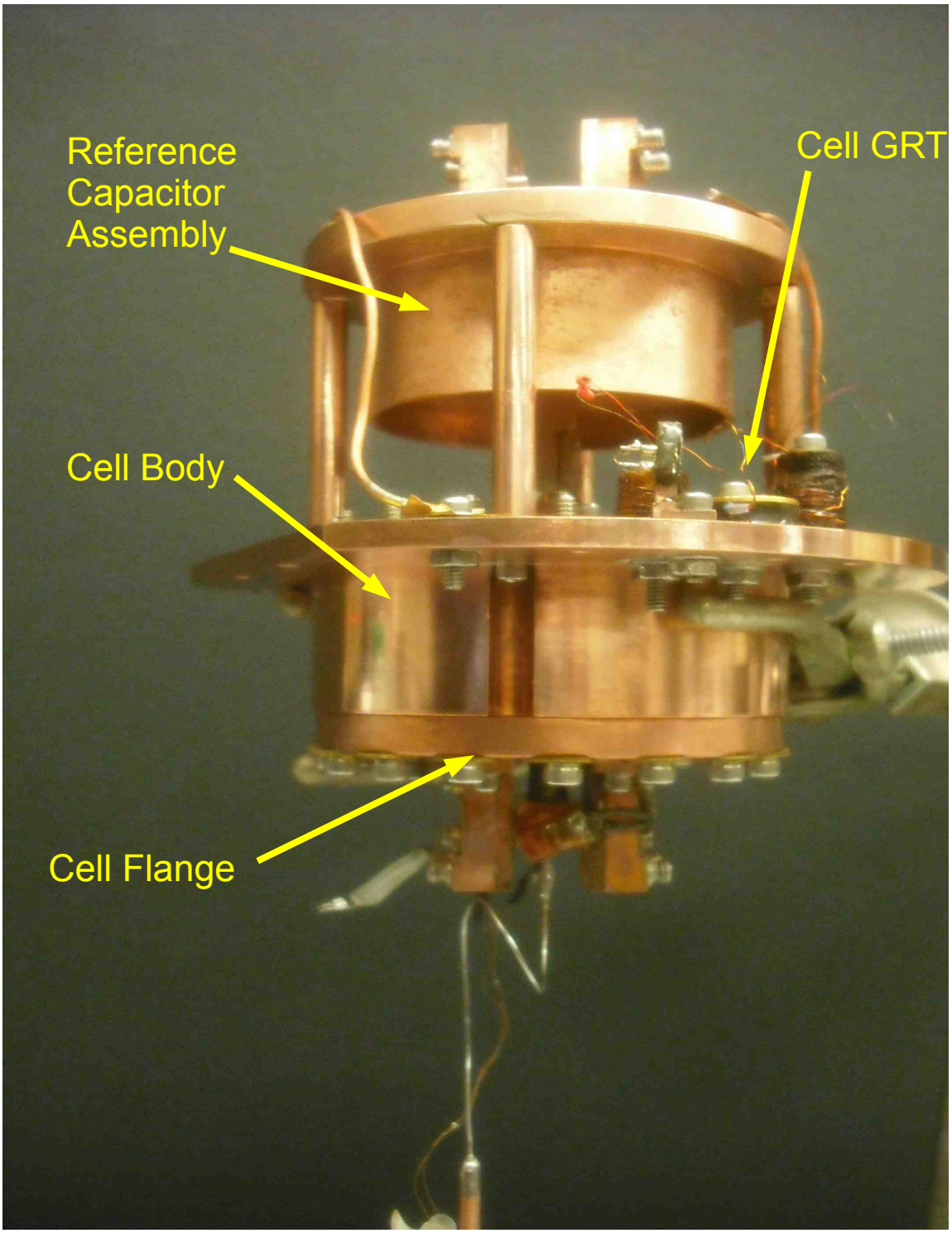

Figure A.5: Picture of the experimental cell in the orientation for joining to the experimental stage, see Figure A.4. The primary visible components are labeled.

assembly has four quadrants(see Figures 3.4 and A.6) electrodes. These electrodes are opposite the primary electrode. This geometry is used in order to probe the helium films with third sound. As well, it allow the investigation of potential systematic errors from tilt, particle contamination, or capillary wetting of the gap. In this way, the different quadrants act as a control on the measurements we are making. By measuring the film thickness change on multiple quadrants, we are able to exclude these possible sources of film thickness change. A duplicate electrode assembly is fabricated and mounted in the reference capacitor assembly, see Figure A.5. It is used for the bridge circuit measurement described in Section ??.

The electrodes are potted with Stycast 1266 into the electrode supports. The electrode supports are grounded to minimize cross talk between quadrants. As well, the supports are used to set the gap between the opposing electrodes. Once the electrode assemblies are fabricated, the surfaces are diamond turned to achieve a nanometer scale surface roughness[3], see Figure A.6. This is critical fabrication step since the films we are measuring are on the order of 30 nm thick. Using an AFM we are able to determine that the surface roughness is less than 10 nm. A relief channel is machined out of the region surrounding the electrodes to forestall capillary filling of the gap, see Figures 3.4 and A.6. The gap is set by placing a spacer of 60 μm thick Kapton film between the electrode holders. The area of a quadrant electrodes is 1 cm^2. Thus the empty cell capacitance of a quadrant is approximately 15 pF.

The electrode assembly is mounted on the cell flange, see Figure A.7. The gap between the cell flange and the assembly is where the majority of the liquid helium in the cell is contained. The gap height is about 3 mm. The film thickness is changes by changing the height of the bulk helium in the cell. The interior volume of the cell body is minimized (approximately 10 cc) in order to minimize

[3]The diamond turning step is performed by KAF manufacturing.

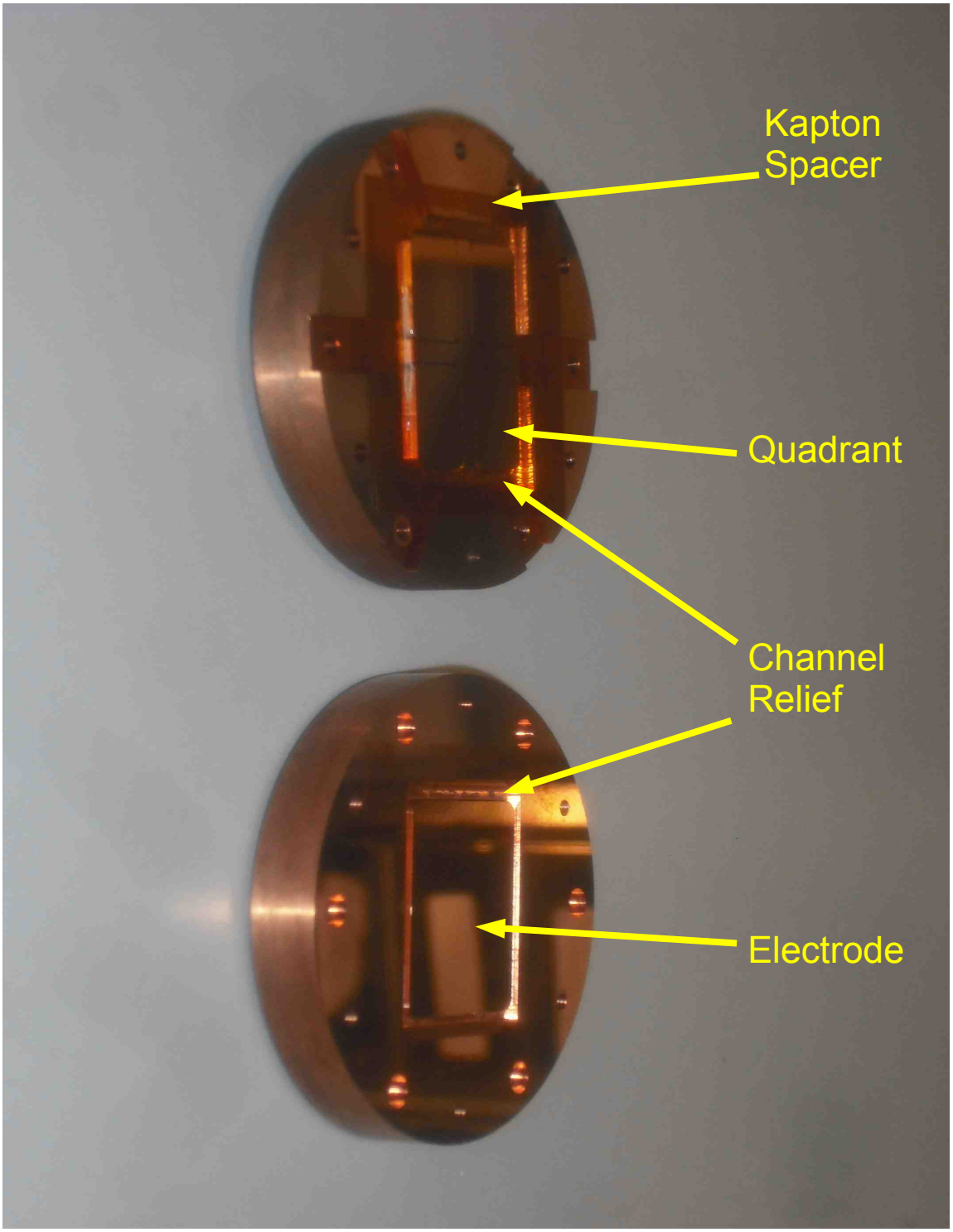

Figure A.6: Picture of the electrode assembly. The assembly is fabricated at UCLA and sent out for the final step of diamond turning of the faces. The mirror-like quality of the surfaces can be seen in the picture.

the change in the capacitance signal during temperature sweeps from condensation/evaporation of the liquid helium in the cell caused by the changing vapor pressure. We estimate that the change in film thickness caused by the change in film height is less than 0.1 Å over the full range of temperature measured in the experiment.

The cell component are cleaned and assembled in a class 100 clean room[4] to minimize particulates within the cell. Additionally, the interior side of the fill line to the cell is terminated with a 5 micron sintered filter disk to prevent large particulates from entering the cell post assembly, see Figure A.8. The cell fill line is routed through a pressure actuated cold valve thermally anchored to the cell, see Figure A.4. The cold valve is closed each time the cell is dosed with helium during the run. This ensures that thermomechanical effects along the fill line do not perturb the helium within the cell. The cell fill line enters the cell through the λ stage. The λ stage is integrated into the cell flange to accurately determine the location of the λ transition in our system, see Figure A.8.

The λ stage consists of a copper block on the end of a quarter inch diameter thin walled stainless steel tube, see Figure A.8. This forms a volume that contains a 0.25 cc volume of LHe. When the cell crosses the λ point in temperature, a discontinuity is registered in the resistance between the thermometers attached to the cell and the λ stage. This is caused by the diverging heat capacity of the helium in the cell at the λ point. Since the connection between the copper block and the cell is made from a thin walled tube of stainless steel, the thermal link between the λ stage and the cell is primarily through the LHe in the tube. Thus, the λ stage can be used as a fixed point for the thermometry calibration. The λ point is know to 10 μK for the system. The limit on the certainty for T_λ is from the uncertainty in the measurement of temperature for the cell GRT.

The cold valve is a critical component of the experimental cell because it

[4]UCLA Nanoelectronics Research Facility

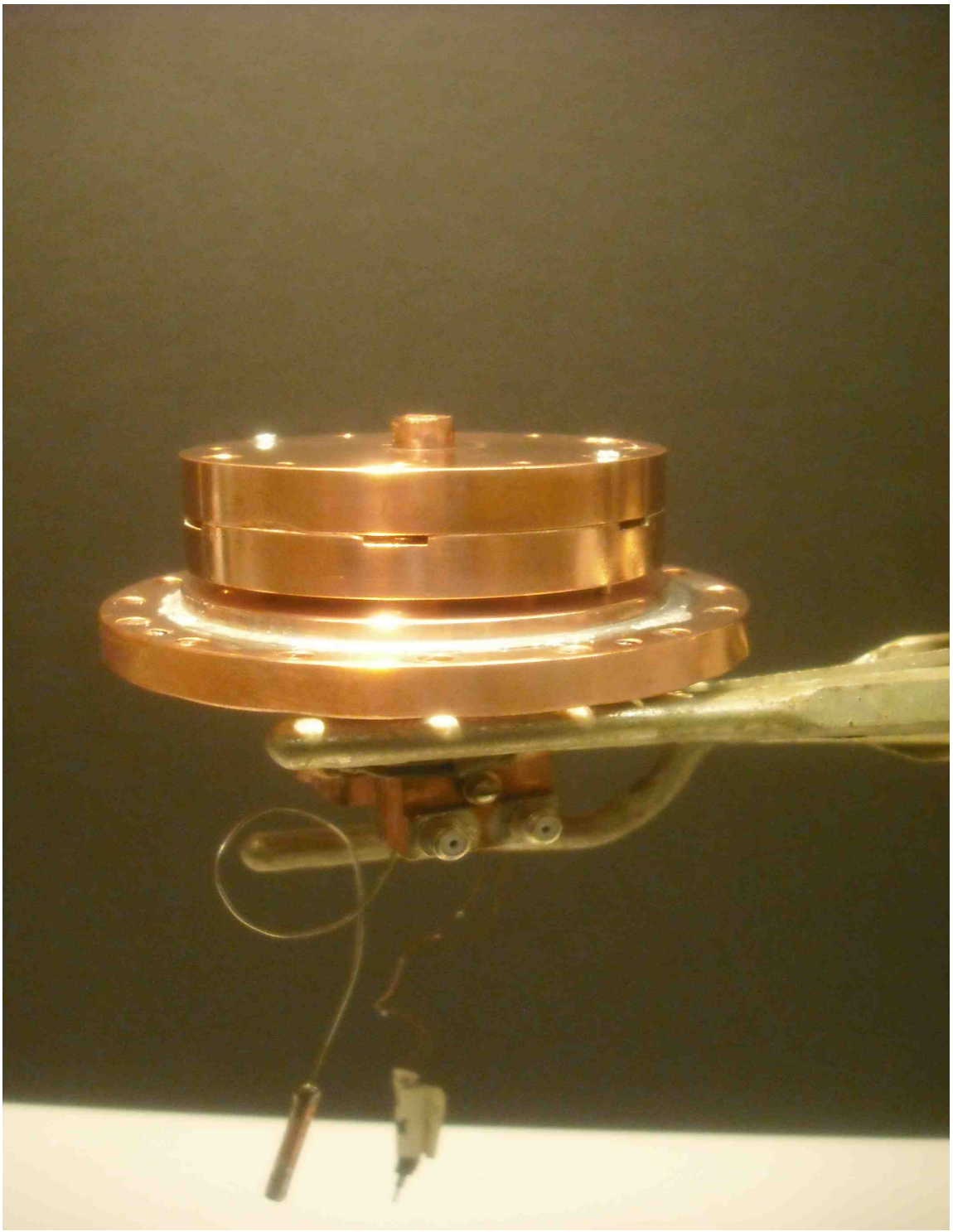

Figure A.7: Picture of the electrode assembly mounted on the cell flange. The gap between the cell flange and the assembly is filled with liquid helium during the experimental run. The cell fill line is visible at the bottom of the flange.

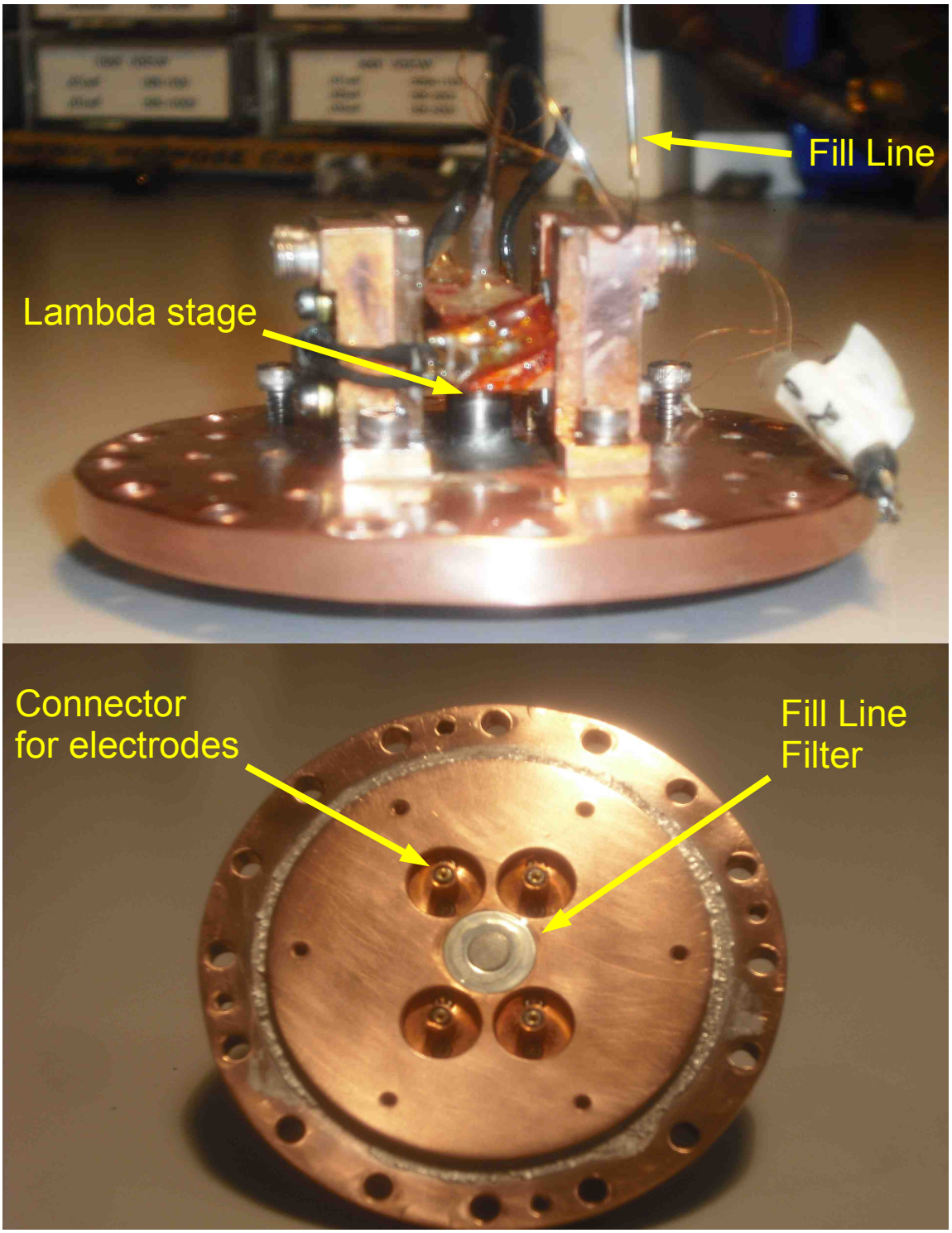

Figure A.8: Pictures of the cell flange. The profile of the λ stage is displayed in the upper panel. Flanking the λ stage are feedthroughs to connect to quadrant electrodes. In the bottom pane the underside of the cell flange is displayed.

isolates the cell once it is charged with a ^{4}He fill. If the cell is not isolated, then the ^{4}He in the cell will form a film in the fill line which will thermally connect the cell to other parts of the cryostat. Thus it would introduce a thermal gradient in the system. The design of the cold valve is based on a published design[69]. The cold valve consists of a flow side and an actuation side, see Figure A.9. When pressure is introduced on the actuation side, a stainless steel diaphragm is deflected. Its deflection forces a torlon needle to press against a seat, thus isolating the cell from the fill line. The valve is normally open and is closed with a minimum of 120 PSI of pressure. Upon running the system, it was discovered that when the valve is operated on the lower end of the operating range of pressure, a heat load introduced on the cell. The origin of the load may be from coupling the cell to the bath through the cold valve actuation line. This problem was resolved by operating the valve at 450 PSI in order to solidify the helium in the actuation line. See Figure A.9 for a schematic of the valve.

Two measurement configurations are used in the experiment; a capacitance bridge to measure film thickness and a capacitive third sound generation with charged bias detection scheme. The capacitance bridge measurement is described in Section **??**. This technique allows the for sub-Å resolution of film thickness changes over long periods of time. While, the third sound generation and detection configuration is described in Section 3.3. Essentially, the technique is to drive one electrode with a sinusoidal electrical potential while detecting the response on a diagonal electrode using the charged bias detection technique described in Reference [5].

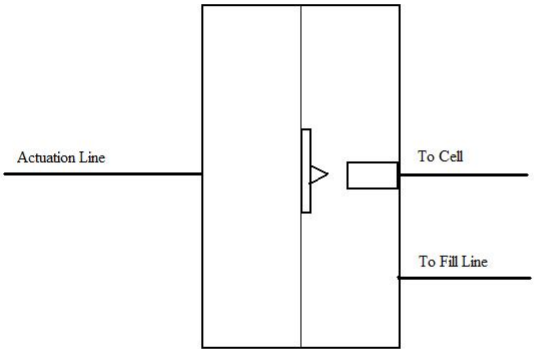

Figure A.9: Diagram of the Cold Valve.

APPENDIX B

Depletion of ρ_s in Thick Films

As mentioned earlier in Section 2.1.3, there are two components which determine the depletion layer; the Van der Waals pressure in the film, and the coherence length. We have developed a model of the pressure in the film based on the exponential atmosphere model [70]. Following that model, a simple differential equation can be used to describe the derivative of the pressure in the film in terms of the Van der Waals force of the substrate on the film;

$$\frac{dP}{dz} = -f_{vdW}(z)\rho(z,P) \tag{B.1}$$

Assume a simple form for ρ, namely, the height variation in rho is simply from the pressure and that ρ is a linear function of pressure. The Van der Waals force is a know expression of the film height[2]. So, the differential equation becomes

$$\frac{dP}{dz} = -\frac{\gamma_0 d_0(3d_0+4z)}{z^4(z+d_0)^2}\left(\rho_0 + \alpha P(z)\right) \tag{B.2}$$

This equation can be solved numerically using the boundary condition that the pressure far from the film is zero. The solution of Equation B.2 gives the pressure in the film as a function of height. From the know properties of Helium [2], a function can be constructed to describe the phase boundary of He II in the Pressure, Temperature plane. This phase boundary includes the solid layer and the pressure induced normal layer (above the lower λ point, 1.76 K). Using the equations, the pressure induced depletion layer as a function of temperature can

be interpolated.

The other contribution to the depletion layer comes from the healing length[40, 41, 27]. The healing length is the length over which the superfluid density recovers to the bulk value near a boundary. The healing length is proportional to the bulk coherence length, the constant of proportionality depends on the boundary conditions. From previous measurements [28], the bulk coherence length is

$$\xi = \xi_0 t^{-1/\nu} \tag{B.3}$$

where $\xi_0 \approx 3.5$

A, t is the reduced temperature, and $\nu = 2/3$. Using the numerical model of the pressure effects and the healing length, we plot $\frac{\bar{\rho_s}}{\rho_s}$ in figure 2.7.

APPENDIX C

Boundary Attenuation Model

In order to model the attenuation at the boundary, we model the problem as a transmission and reflection problem. We model the boundary as the edge of the substrate. At the substrate edge, the film surface follows the curvature of the substrate edge. The curvature of the film surface increases the free energy at the surface. Using the surface tension of Helium, we can estimate the contribution to the surface energy from the boundary.

$$U_{boundary} \approx \alpha(T) r \tag{C.1}$$

where α is the surface tension and r is the radius of curvature of the film edge. We estimate that r is of the order of 10 μm based on the roughness of the edge. We can then include this term into the expression which determines the equilibrium film thickness and use this to estimate the thinning of the film on the boundary,

$$mgh = \frac{\gamma_0}{d^3}\left(1 + \frac{d}{d_{1/2}}\right)^{-1} + U_{boundary} \tag{C.2}$$

In this expression, γ_0 is the Van der Waals acceleration constant for He on a copper substrate, and $d_{1/2}$ is the corresponding retardation parameter [37]. This contribution acts to lower the film thickness relative to the film on the substrate. The change in film thickness for a 300 Å film is approximately 30 Å. These changes in the force on a He atom at the surface of the film and the film thickness lead to a change in the third sound speed, see Equation 2.7. The ratio of the speed in

the film and at the boundary can be used to calculate a reflection coefficient for the boundary.

$$R = \frac{\left(\frac{c_f}{c_b} - 1\right)^{1/2}}{\left(\frac{c_f}{c_b} + 1\right)^{1/2}} \tag{C.3}$$

where c_f is the third sound speed in the film and c_b is the third sound speed in the boundary. Using these expression we estimate that the reflection coefficient drops by ten percent from 1.5 K to T_λ. The reflection coefficient is inversely proportional to the attenuation. So, we can expect that changes in boundary reflection will lead to an increase of 10 percent to third sound attenuation in the films studied. This does not account for the peak in attenuation which is the primary result of the measurements, Figure 2.8. There is a slight increase of the attenuation from 1.6 to 2 K. This may be explained by the change in reflection coefficient.

APPENDIX D

The Energy of Second Sound

Within tens of μK of the λ transition, there is a step in the film thickness which scales with Van der Waals energy of the film, see Fig. 3.10. This step is only observable when the thermal sweep rate is extremely small, μK per hour. That the sweep rate must be so small points away from a non-equilibrium source of film thickening such as the thermomechanical effect. The film in this temperature regime is completely normal and is far from it's transition temperature. In terms of what is occurring in the cell, the most significant element is the bulk Helium in the cell which is undergoing the λ transition. We can conjectured that the energy driving the change in the film thickness arises from a bulk phenomena and the film is acting as a probe of the bulk.

In this appendix, we will explore the possibility that the onset of thermally excited second sound modes in the bulk is responsible for the step in film thickness observed at the λ transition. In the following calculation, we will use second sound data from the hydrodynamic regime to model the bulk free energy.

D.1 Debye Calculation

We can model the system as a Debye solid. The expression for the free energy per unit volume of the sound modes for the Debye solid model is

$$FE = \frac{3K_BT}{(2\pi C)^3}\int_0^{\omega_D}\omega^2 ln\left(1-e^{-\frac{\hbar\omega}{k_BT}}\right)d\omega \tag{D.1}$$

where C is the speed of sound [71], the limit of integration is the Debye frequency, ω_D and the other terms have their usual connotations. For our calculation, we are interested in the free energy of the second sound modes for 1 cc of bulk ^{4}He. The expression becomes

$$FE_2(T) = \frac{3VK_BT}{(2\pi C_2(T))^3} \int_0^{\omega_D(T)} \omega^2 ln\left(1 - e^{-\frac{\hbar\omega}{k_BT}}\right) d\omega \tag{D.2}$$

where V is 1 cc, $C_2(T)$ is the speed of second sound explicitly noting the temperature dependence and the remaining terms have the same meaning. We can estimate the Debye frequency cut-off using the second sound speed and the damping coefficient for second sound, $D_2(T)$ with units of cm^2/s. We take the Debye frequency to be

$$\omega_D = \frac{C_2^2}{D_2} \tag{D.3}$$

In order to calculate the free energy, we introduce the change of variable,

$$x_D = \frac{\hbar\omega_D}{k_BT} \tag{D.4}$$

the expression for the free energy becomes,

$$FE_2(T) = \frac{3V(K_BT)^4}{C_2(T)^3\hbar^3 2\pi^2} \int_0^{x_D} x^2 ln\left(1 - e^{-x}\right) dx \tag{D.5}$$

Using data for D_2 from Ref. [64] and data for C_2 from [2], we can now calculate the free energy using a suitable mathematical program. The result of such a calculation is presented in Fig. D.1. It fails to represent the phenomena we observe because as the temperature decreases to far below the λ point, the free energy gets much larger than a few ergs. For this model to be reasonable, there must be some second sound modes in the film to drive the energy difference between the film and the bulk to zero when the system is far from the λ point.

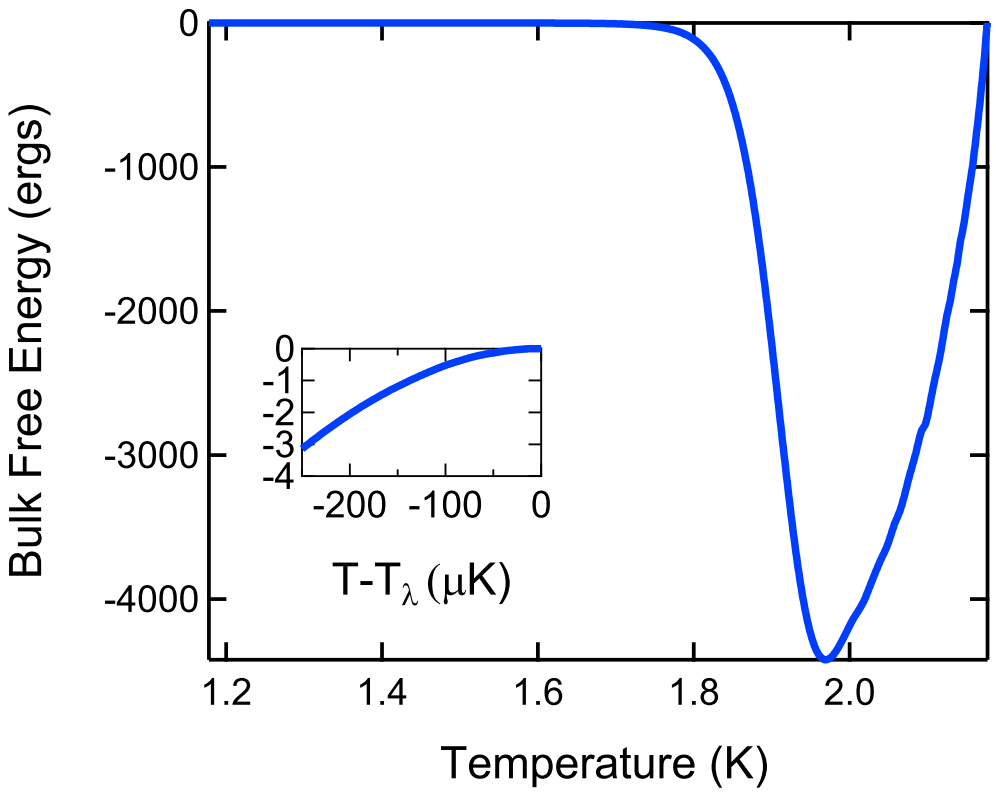

Figure D.1: Plot of the bulk free energy using Eq. D.5. The insert is the same curve close to T_λ.

We develop an expression for the free energy in the film. The leading term will be the same for the film and the bulk. The difference will lie in the limits of the integration. Second sound modes in the film are limited by the viscous penetration depth, Eq. 2.1. We expect that low frequency second sound will be damped out in the film when the viscous penetration depth is on the order of the film thickness. We can use the film thickness to set the cut off frequency in the film by using the viscous penetration depth expression.

$$\omega_C = \frac{2\eta}{\rho\Gamma d^2} \tag{D.6}$$

In this expression, η is the viscosity, d is the film thickness, and ρ is the density. We introduce the term Γ in the expression as a tuning parameter. Since we do not know exactly the ratio of the film thickness to the viscous penetration depth at the cut-off, we introduce this tuning parameter and expect it to be on the order of one. The spectrum of second sound in the film would range from the cut-off frequency to the debye frequency. Taking the difference of the two integrals would result in changing the limits of integration. Instead of integrating from 0 to ω_D, we would integrate from ω_D to ω_C. Thus, we wound find the difference in energy between the second sound modes in the film and in the bulk to be

$$\Delta FE_2(T) = \frac{3V(K_BT)^4}{C_2(T)^3\hbar^3 2\pi^2}\int_{x_C}^{x_D} x^2 ln\left(1-e^{-x}\right)dx \tag{D.7}$$

With the choice of Γ=3, the result is plotted in Fig. D.2.

The issue of the energy difference far from the λ point seems to be resolved by adding modes to the film. The energy difference has a very sharp fall off and is thus consistent with our experimental data. The issue that remains with the model is that there are practically no modes in the bulk near T_λ. The energy difference of a few ergs between the bulk and the film is from modes in the film. Close to T_λ, $x_C > x_D$. This is not a physically meaningful result.

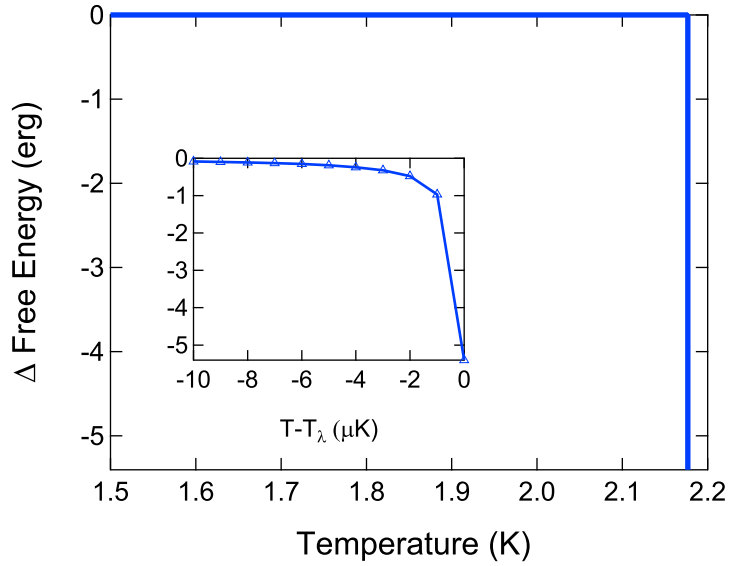

Figure D.2: Plot of the free difference energy using Eq. D.7. The insert shows the free energy difference close to T_λ.

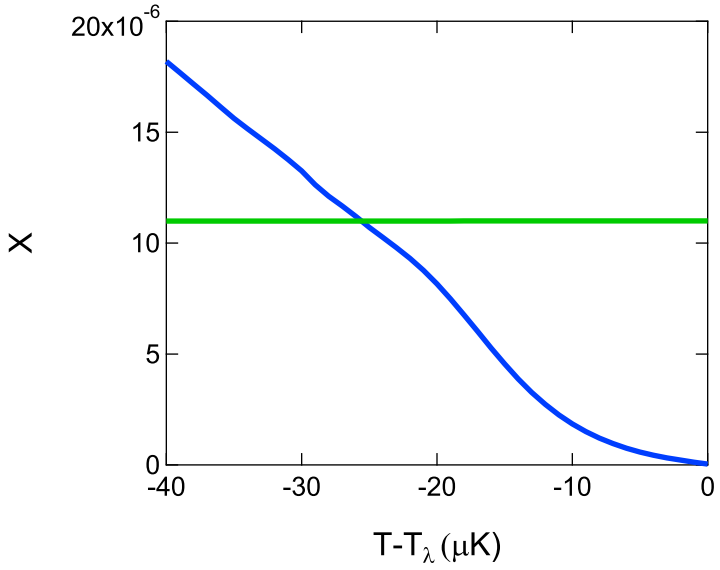

Figure D.3: Plot of the Debye cutoff in blue and the viscous penetration depth cutoff in green close to the λ point.

Alternatively, we can return to Eq. D.5 to see at what temperature the free energy of the bulk is on the order of an erg. This could be the temperature at which there is onset of second sound in the film. In this way, second sound modes in the film would drive the free energy difference to zero below the threshold temperature. While above the threshold, second sound does not propagate in the film. From inspecting the insert for Fig. D.1, the threshold temperature would be approximately 100 μK. This is on the order the onset temperature we observe.

APPENDIX E

Equilibration Time

In our measurements of the critical Casimir step at T_λ, the film takes approximately 10 hours to equilibrate. Since the film is above T_{KT}, a much longer equilibration time is to be expected since Helium atoms will no longer be transported through the film in response to chemical potential gradients. Since this channel for transport is closed, the only remaining channel is through the vapor. As a first step to quantifying the expected time to equilibrium, we model the system as a drift potential imposed on a thermal system where $K_B T >> U_{drift}$. From the Einstein diffusion relation and the properties of the ^{4}He vapor, we can get a time constant [71].

$$\mu = \frac{D}{KT} = \frac{v_{drift}}{F_{drift}} \tag{E.1}$$

From the vapor properties we can estimate the diffusion constant. From the Van der Waals energy change corresponding to the step we can estimate the drift force. The diffusion constant can be estimated using the mean free path and the thermal velocity;

$$D \approx \lambda v_{thermal} = 5 \times 10^{-2} cm^2/s \tag{E.2}$$

Where $\lambda = 4 \times 10^{-6} cm$ and $v_{thermal} = 1.2 \times 10^4 cm/s$

$$F_{drift} = \frac{\Delta U_{vdw}}{\Delta X} \tag{E.3}$$

$\Delta X = .1cm$ is the distance from the bulk to the film and $\Delta U_{vdw} = 1\mu K$. Rearranging;

$$\tau_{drift} = \frac{(\Delta X)^2(KT)}{(\Delta U)D} \approx 10^5 seconds \tag{E.4}$$

The result is an order of magnitude too large. Improving the model can be done through refining the model of the diffusion constant E.2. This is a first step for understanding the length of time necessary to achieve the equilibrium film thickness value when the system is near T_λ.

References

[1] H. B. G. Casimir, "On the attraction between two perfectly conducting plates," *Proc. K. Ned. Akad. Wet. Ser. B: Phys. Sci.*, vol. 51, p. 793, 1948.

[2] R. J. Donnelly and C. F. Barenghi, "The observed properties of liquid helium at the saturated vapor pressure," *J. Phys. Ref. Data*, vol. 27, p. 1217, 1998.

[3] H. A. Kierstead, "Lambda curve of liquid He^4," *Phys. Rev.*, vol. 162, p. 153, 1967.

[4] C. A. Swenson, "The liquid-solid transformation in helium near absolute zero," *Phys. Rev.*, vol. 79, p. 626, 1950.

[5] J. A. Hoffmann, K. Penanen, J. C. Davis, and R. E. Packard, "Measurements of attenuation of third sound: Evidence of trapped vorticity in thick films of superfluid ^{4}He," *J. Low Temp. Phys.*, vol. 135, p. 177, 2004.

[6] K. Penanen, J. A. Hoffmann, J. C. Davis, and R. E. Packard, "Effect of He-3 on third sound attenuation in thick He-4 films," *J. Low Temp. Phys.*, vol. 134, p. 1069, 2004.

[7] D. Bergman, "Third sound in superfluid helium films of arbitrary thickness," *Phys. Rev. A.*, vol. 3, p. 2058, 1971.

[8] D. R. Nelson and J. M. Kosterlitz, "Universal jump in the superfluid density of two-dimensional superfluids," *Phys. Rev. Lett.*, vol. 39, p. 1201, 1977.

[9] O. Vasilyev, A. Gambassi, A. Maciolek, and S. Dietrich, "Universal scaling functions of critical Casimir forces obtained by Monte Carlo simulations," *Phys. Rev. E*, vol. 79, p. 041142, 2009.

[10] R. Garcia and M. H. W. Chan, "Critical fluctuation-induced thinning of ^{4}He films near the superfluid transition," *Phys. Rev. Lett.*, vol. 83, p. 1187, 1999.

[11] A. Ganshin, S. Scheidemantel, R. Garcia, and M. H. W. Chan, "Critical casimir force in ^{4}He films: Confirmation of finite-size scaling," *Phys. Rev. Lett.*, vol. 97, p. 075301, 2006.

[12] R. Zandi, A. Shackell, J. Rudnick, M. Kardar, and L. P. Chayes, "Thinning of superfluid films below the critical point," *Phys. Rev. E*, vol. 76, p. 030601, 2007.

[13] A. Maciolek, A. Gambassi, and S. Dietrich, "Critical Casimir effect in superfluid wetting films," *Phys. Rev. E*, vol. 76, p. 031124, 2007.

[14] A. Hucht, "Thermodynamic casimir effect in ^{4}He Films near T_λ: Monte Carlo Results," *Phys. Rev. Lett.*, vol. 99, p. 185301, 2007.

[15] M. Hasenbusch, "The specific heat of thin films near the λ-transition: a Monte Carlo study of an improved three-dimensional lattice model," *J. Stat. Mech.: Theory Exp.*, p. P02005, 2009.

[16] M. Krech and S. Dietrich, "Specific heat of critical films, the Casimir force, and wetting films near critical end points," *Phys. Rev. A*, vol. 46, p. 1922, 1992.

[17] F. M. Gasparini, M. O. Kimball, K. P. Mooney, and M. Diaz-Avila, "Finite-size scaling of ^{4}He at the superfluid transition," *Rev. Mod. Phys.*, vol. 80, p. 1009, 2008.

[18] R. Z. J. Rudnick and M. Kardar, "Casimir Forces, Surface Fluctuation, and Thinning of Superfluid Film," *Phys. Rev. Lett.*, vol. 93, p. 155302, 2004.

[19] R. Garcia, S. Jordan, J. Lazzaretti, and M. H. W. Chan, "Quartz microbalance study of thick ^{4}He film near the superfluid transition," *J. Low Temp. Phys.*, vol. 134, p. 527, 2004.

[20] V. M. Mostepaneko and N. N. Trunov, *The Casimir Effect and its Applications*. Oxford Science Publications, 1997.

[21] G. L. Klimchitskaya, U. Mohideen, and V. M. Mostepanenko, "The Casimir force between real materials: Experiment and theory," *Rev. Mod. Phys.*, vol. 81, p. 1827, 2009.

[22] M. Krech, *The Casimir Effect in Critical Systems*. World Scientific Publishing Co. Pte. Ltd., 1994.

[23] F. London, *Superfluids Volume II Macroscopic Theory of Superfluid Helium*. Dover Publications, Inc., 1954.

[24] K. R. Atkins, *Liquid Helium*. Cambridge University Press, 1959.

[25] C. Enss and S. Hunklinger, *Low-Temperature Physics*. Springer, 2005.

[26] K. G. Wilson, "Renormalization group and critical phenomena. i. renormalization group and the Kadanoff scaling picture," *Phys. Rev. B.*, vol. 4, p. 3174, 1971.

[27] P. C. Hohenberg, A. Aharony, B. I. Halperin, and E. D. Siggia, "Two-scale-factor universality and the renormalization group," *Phys. Rev. B*, vol. 13, p. 2986, 1976.

[28] R. P. Henkel, E. N. Smith, and J. D. Reppy, "Temperature dependence of the superfluid healing length," *Phys. Rev. Lett.*, vol. 23, p. 1276, 1969.

[29] D. S. Greywall and G. Ahlers, "Second-sound velocity, scaling, and universality in He II under pressure near the superfluid transition," *Phys. Rev. Lett.*, vol. 28, p. 1251, 1972.

[30] M. N. Barber in *Phase Transitions and Critical Phenomena* (C. Domb and J. L. Lebowitz, eds.), vol. 8, ch. 2, pp. 146–265, New York: Academic Press, 1983.

[31] D. R. Nelson in *Phase Transitions and Critical Phenomena* (C. Domb and J. L. Lebowitz, eds.), vol. 7, ch. 1, pp. 1–100, New York: Academic Press, 1983.

[32] R. W. A. van de Laar, A. van der Hock, and H. van Beelen, "Two-dimensional behaviour of very thin ^{4}He films on glass," *Physica B*, vol. 216, p. 24, 1995.

[33] I. Rudnick, "Critical surface density of the superfluid compnent in ^{4}He films," *Phys. Rev. Lett.*, vol. 40, p. 1454, 1978.

[34] V. Ambegaokar, B. I. Halperin, D. R. Nelson, and E. D. Siggia, "Dynamics of superfluid films," *Phys. Rev. B*, vol. 21, p. 1806, 1980.

[35] J. K. Perron and F. M. Gasparini, "Critical point coupling and proximity effects in ^{4}He at the superfluid transition," *Phys. Rev. Lett.*, vol. 109, p. 035302, 2012.

[36] N. Schultka and E. Manousakis, "Crossover from two- to three-dimensional behavior in superfluids," *Phys. Rev. B*, vol. 51, p. 11712, 1995.

[37] E. Cheng and M. W. Cole, "Retradation and many-body effects in multilayer-film adsorption," *Phys. Rev. B*, vol. 38, p. 987, 1988.

[38] V. Privman and M. E. Fisher, "Universal critical amplitudes in finite-size scaling," *Phys. Rev. B*, vol. 30, p. 322, 1984.

[39] K. R. Atkins, "Third and fourth sound in liquid helium II," *Phys. Rev.*, vol. 113, p. 962, 1959.

[40] I. Rudnick and J. C. Fraser, "Third sound and the superfluid parameters of thin helium films," *J. Low Temp. Phys.*, vol. 3, p. 225, 1970.

[41] J. H. Schlotz, E. O. McLean, and I. Rudnick, "Third sound and the healing length of He II in films as thin as 2.1 atomic layers," *Phys. Rev. Lett.*, vol. 32, p. 147, 1974.

[42] K. L. Telschow, R. K. Galkiewicz, and R. B. Hallock, "Experiments on the attenuation of third sound in saturated superfluid helium films," *Phys. Rev. B.*, vol. 14, p. 4883, 1976.

[43] H. Lamb, *Hydrodynamics*. Dover, 1945.

[44] D. Bergman, "Hydrodynamics and third sound in thin He II films," *Phys. Rev.*, vol. 188, p. 370, 1969.

[45] H. B. Callen, *Thermodynamics and an Introduction to Thermostatistics*. John Wiley and Sons, 1985.

[46] S. J. Putterman, R. Finkelstein, and I. Rudnick, "Macroscopic quantum uncertainty principle and superfluid hydrodynamics," *Phys. Rev. Lett.*, vol. 27, p. 1697, 1971.

[47] M. Chester and R. Maynard, "Microscopic origin for the apparent uncertainty principle governing the anomalous attenuation of third sound," *Phys. Rev. Lett.*, vol. 29, p. 628, 1972.

[48] K. Penanen and R. E. Packard, "A model for third sound attenuation in thick He-4 films," *J. Low Temp. Phys.*, vol. 128, p. 25, 2002.

[49] J. A. Hoffmann, *Superfluid ^{4}He: On sin ϕ Josephson Weak Links and Dissipation of Third Sound*. PhD thesis, University of California, Berkeley, 2005.

[50] V. L. Ginzburg and L. P. Pitaevski, "On the theory of superfluidity," *Soviet Physics JETP*, vol. 34, p. 858, 1958.

[51] M. Chester and L. Eytel, "Some calculations regarding the characteristic length for superfluidity in liquid helium," *Phys. Rev. B*, vol. 13, p. 1069, 1976.

[52] T. Oestereich and H. Stenschke, "Density profile of an adsorbed helium film," *Phys. Rev. B*, vol. 16, p. 1996, 1977.

[53] A. M. R. Schechter, R. W. Simmonds, and J. C. Davis, "Capactive generation and detection of third sound resonances in saturated superfluid ^{4}He films," *J. Low Temp. Phys.*, vol. 110, p. 603, 1998.

[54] D. R. Luhman and R. B. Hallock, "Third sound on CaF_2 films of varying roughness," *Phys. Rev. B.*, vol. 74, p. 014510, 2006.

[55] R. C. Richardson and E. N. Smith, *Experimental Techniques in Condensed Matter Physics at Low Temperatures*. Addison-Wesley Publishing Company, 1988.

[56] G. A. Williams, "Dimensionality crossover of the ^{4}He superfluid transition in a slab geometry," *J. Low Temp. Phys.*, vol. 101, p. 415, 1995.

[57] D. J. Bishop and J. D. Reppy, "Study of the superfluid transition in two-dimensional ^{4}He films," *Phys. Rev. Lett.*, vol. 40, p. 1727, 1978.

[58] R. Garcia, *Fluctuation-induced forces in ^{4}He films near the superfluid transition*. PhD thesis, The Pennsylvania State University, 1999.

[59] R. J. Dionne and R. B. Hallock in *Quantum Fluids and Solids-1989* (G. Ihas and Y. Takano, eds.), vol. 194, pp. 199–200, New York: AIP, 1989.

[60] G. A. William, "Vortex loops in the critical Casimir effect in superfluid and superconducting films," *Physica C*, vol. 404, p. 415, 2004.

[61] M. Hasenbusch, "Specifc heat, internal energy, and thermodynamic Casimir force in the neighborhood of the λ transition," *Phys. Rev. B*, vol. 81, p. 165412, 2010.

[62] G. W. Swift, *Determination of the dielectric anisotropy in superfluid ^{3}He-A*. PhD thesis, University of California, Berkeley, 1980.

[63] G. A. Williams, "Attenuation of superfluid 2-phase sound," *J. Low Temp. Physics*, vol. 50, p. 455, 1983.

[64] R. A. Ferrell and J. K. Bhattacharjee, "Viscous damping of second sound near the Lambda point of liquid ^{4}He," *Phys. Rev. Lett.*, vol. 51, p. 487, 1983.

[65] P. C. Hohenberg and B. I. Halperin, "Theory of dynamic critical phenomena," *Rev. Mod. Phys.*, vol. 49, p. 435, 1977.

[66] J. A. Tarvin, F. Vidal, and T. J. Greytak, "Measurements of the dynamic structure factor near the lambda temperature in liquid helium," *Phys. Rev. B*, vol. 15, p. 4193, 1977.

[67] J. W. Ekin, *Experimental Techniques for Low-Temperature Measurements*. Oxford University Press, 2006.

[68] L. E. DeLong, O. G. Symko, and J. C. Wheatley, "Continuously Operating ^{4}He Evaporation Refrigerator," *Rev. Sci. Instrum.*, vol. 42, p. 147, 1971.

[69] N. Bruckner, S. Backhaus, and R. Packard, "An improved low temperature valve," *Czech. J. Phys.*, vol. 46, p. 2741, 1996.

[70] D. V. Schroeder, *An Introduction to Thermal Physics*. Addison Wesley Longman, 2000.

[71] F. Schwabl, *Statistical Mechanics*. Springer, 2002.